N90-25992

von Karman Institute for Fluid Dynamics

Lecture Series 1990–02

GAS TURBINE COMBUSTION

February 19–23, 1990

SUPERSONIC COMBUSTOR MODELING

D.W. Riggins, J.P. Drummond, M.H. Carpenter

NASA-Langley Research Center, USA

Supersonic Combustor Modeling

D. W. Riggins[*]
J. Philip Drummond[†]
Mark H. Carpenter[‡]

Overview

Research has been undertaken to achieve an improved understanding of physical phenomena present when a supersonic flow undergoes chemical reaction. A detailed understanding of supersonic reacting flows is necessary to successfully develop advanced propulsion systems now planned for use late in this century and beyond. In order to explore such flows, a study was begun to create appropriate physical models for describing supersonic combustion and to develop accurate and efficient numerical techniques for solving the governing equations that result from these models. For this work, a computer program was written to study reacting flows. The program was constructed to consider the multicomponent diffusion and convection of important chemical species, the finite-rate reaction of these species, and the resulting interaction of the fluid mechanics and the chemistry. The program was first used to study a spatially developing and reacting mixing layer, and the results were analyzed to draw conclusions regarding the structure and growth of the evolving layer. The mixing layer provides a basic reacting flow field problem that can be studied, but it also serves as an excellent physical model for the mixing and reaction processes that take place in a scramjet combustor. Following the study of mixing layer development and growth, several techniques were considered to enhance the fuel-air mixing

[*]Research Scientist, Langley Research Center, Hampton, Virginia.
[†]Senior Research Scientist, Langley Research Center.
[‡]Research Scientist, Langley Research Center, Hampton, Virginia.

and growth of that layer to improve its overall combustion efficiency. Several alternate fuel injector configurations were developed from this study that increased the degree of mixing and combustion that could be achieved.

Introduction

Research is currently underway, both in the United States and abroad, to develop advanced aerospace propulsion systems now planned for use late in this century and beyond. One such program is being carried out at the NASA Langley Research Center to develop a hydrogen-fueled supersonic combustion ramjet engine, also known as a scramjet, capable of propelling a vehicle at hypersonic speeds in the atmosphere. One phase of this research has been directed toward gaining a detailed understanding of the complex flow field present in the engine over a range of flow conditions. Numerical modeling of various regions of the engine flow has been shown to be a valuable tool for gaining insight into the nature of these flows. This approach has been used in conjunction with an ongoing experimental program to develop an effective analysis capability [1].

The flow field in a scramjet engine is governed by the Navier-Stokes equations coupled to a system of equations describing each of the species present initially and produced by chemical reaction. The governing equations were solved in prior analyses using either explicit or implicit finite-difference techniques, with the chemical reaction process modeled by an ideal (mixing controlled) reaction model. Using these approaches, analyses of various ramjet and scramjet configurations have been carried out, and trends that were established by experiments have been predicted

Chemical reaction is not mixing controlled throughout a scramjet combustor, however Although chemical reaction may equilibrate in the rearward region of a well-designed combustor, chemistry in the forward portions of the combustor is certainly kinetically controlled. Finite-rate kinetics is, in fact, a critical issue in the design of flameholders in the engine, and this phenomenon must be considered along with the effects of molecular and

turbulent fuel-air mixing to develop an accurate engine flow model. It is for this reason that attention has turned in the present work to a more basic and detailed analysis of chemically reacting flow fields. The long-term purpose of the present research is to develop detailed models for fuel-air mixing and reaction in an engine flow field and to develop accurate and efficient numerical methods for solving the equations governing reacting flow that result from these models.

Because of computer resource limitations, however, detailed modeling of the complete engine problem cannot be considered at the present time. A more tractable problem that relaxes only the complexities introduced by engine geometry is posed by the spatially developing, primarily supersonic, chemically reacting two-dimensional mixing layer. A major portion of the chemical reaction taking place in a supersonic combustor occurs in mixing layers. All the difficulties introduced by the fluid mechanics, combustion chemistry, and interactions between these phenomena are retained by the reacting mixing layer, making it an ideal problem for the detailed study of supersonic reacting flow.

Prior studies on supersonic reacting mixing layers have been quite limited. A fair amount of the work has been carried out, however, on nonreacting mixing layers, both supersonic and subsonic. Even without combustion, the results of these studies provided a significant amount of useful information for understanding reacting layers. Carpenter [4] studied the development of a laminar, free-shear layer behind steps and blunt bodies over a Mach number range of 0 to 10. He concluded that the development of the layer could best be understood in terms of vorticity transfer. The effect of compressibility was to increase the diffusion process in the layer, leading to more rapid development toward asymptotic conditions with increasing Mach number. Brown and Roshko [5] studied the subsonic mixing layer that developed between nitrogen and helium streams and found that the layer was dominated by large-scale coherent vortical structures. They found that these structures tended to convect at a nearly constant speed and that the size of the structures and the space between them changed discontinuously with movement downstream by the

3

joining of those structures with their neighbors. Results of their experiment " suggested that turbulent mixing and entrainment was a process of entanglement on the scale of the large structures." They also found that very large changes in the density ratio (up to 49) measured transversely across the mixing layer had only a small effect on spreading of the layer. The authors concluded, therefore, that the significant reduction in supersonic mixing layer growth rate with increasing Mach number was due primarily to compressibility effects, rather than density effects as had been thought in the past.

The role of coherent structures in turbulent processes in mixing layers was studied further by Roshko [6]. He found that the size of the coherent structures and the spacing between them increased with increasing downstream distance. The vortices were found to travel at a constant speed of $(u_1 + u_2)/2$, where u_1 and u_2 are the free-stream velocities of the two streams making up the layer. Each vortex also had a finite life span that began and ended abruptly. Coincident with two or more of these endings, a new lifespan began with two or more vortices coalescing to form a new larger vortex. As noted above, each of these vortices was observed to move at a nearly constant speed, resulting in a fairly constant spacing between vortex and its neighbor as they moved downstream during their lifetime. Developed mixing layers are self-similar, however, requiring that the spacing between vortices should increase linearly in the mean with increasing downstream distance. Roshko resolved this contradiction by reasoning that changes in the layer must occur discontinuously and irregularly along the layer such that the scale of the structure grew smoothly and linearly in the mean. Roshko further found that in the transition region of the layer, there was only one spacing distance between neighboring vortices, and this spacing represented the most stable wavelength selected by the laminar portion of the layer. In this region the scale had not yet become dispersed, as they did further downstream in the turbulent regime. Also, three-dimensional effects had not come into play in the transition region. Finally, Roshko noted that mixing layer growth likely occurred near or during the pairing event. Entrainment brought together "pieces" of fluid from either side of the layer,

also enhancing the mixing process. Between each of these pairing/entrainment events, the vortices appeared to convect in an apparently passive fashion.

Ferziger and McMillian [7] in studies of the structure in turbulent shear flows also noted the presence of coherent structures and pairing in a developing mixing layer. They went on to discuss the importance of a tearing mechanism where vortices tended to be torn apart by shearing and then redistributed in parts to their neighboring vortices. They also pointed out the importance of three-dimensional effects in destabilizing the layer. The coherent structures present in the mixing layer tended to be unstable to three-dimensional perturbation that destroyed the spanwise coherence of the structures. Finally, the authors also noted that three-dimensional effects could also be introduced by streamwise vorticity produced by the stretching of vortical structures.

There has been additional work in the literature describing important structures present in developing mixing layers, but the authors have gone on to seek specific mechanisms leading to the production of the structures and their effect on the flow. Several of these authors have dealt particularly with mechanisms associated with retardation of mixing in the supersonic development of layers. Oh [8] hypothesized that when the local Mach number exceeded 1, some fraction of the turbulence energy in the flow was generated by shocks that formed about the eddies (eddy shocks). These shocks were quite weak, differing little from Mach waves, but having finite strength. Some of the eddies in the flow were decelerated by passing through these shocks, and the resulting disturbances produced pressure fluctuations. These fluctuations appeared to correlate well with velocity and density fluctuations in the flow. Favorable correlations in fluctuations of pressure and velocity gradient gave rise to values of the pressure dilation term $p'\partial u'_j/\partial x_j$ that acted as a source or sink of turbulent kinetic energy in the flow. This term vanished in incompressible flows and in low-speed mixing flows where there was a large density variation. The term took on larger values, however, in high Mach number free-mixing layers and acted as a turbulent kinetic energy sink when gradients of mean Mach number and density had the

5

same sign. Therefore, Oh reasoned that the pressure dilation term could act to reduce the turbulent shear level in high Mach number mixing layers, thereby slowing the growth of the layer relative to the incompressible case. This effect agreed with the results cited earlier in this chapter. Oh then carried out calculations by using these ideas that appeared to validate his hypothesis. Papamoschou and Roshko [9] also observed that the spreading rate of compressible mixing layers was significantly reduced over that of incompressible layers, and they attributed that difference to compressibility effects. They deduced from their studies of large-scale structures in the layer that it was appropriate to define a natural coordinate system that moved with these structures. With this system, an alternative Mach number, termed the convective Mach number M_c was defined as $M_c = (u - u_c)/a$, where u is the free-stream velocity, u_c is the convection velocity of the large-scale structures, and a is the local speed of sound. The reduction in mixing layer spreading rate (by approximately a factor of 3 or 4) was shown to correlate well with $M_c \approx 0.5$ and leveling off for $M_c > 1.0$. Reduced spreading therefore seemed to the authors to be due to a stabilizing effect of the convective Mach number.

Hussaini, Collier, and Bushnell [10] offered a possible explanation for the correlation of mixing-layer spreading rate with convective Mach number. Their explanation was tied to the formation of the eddy shocklets that were described earlier. The authors studied numerically the behavior of an eddy convecting subsonically, relative to a locally supersonic flow, with a convective Mach number greater than one. Such flows could therefore support transient shock structures associated with the eddies. As the eddy accelerated in the supersonic flow, an eddy shocklet formed which tended to distort the eddy. As this process continued, an eddy bifurcation occurred, resulting in the formation of a vortex of opposite circulation. Additionally, the length scale of the original vortex was reduced. Therefore, it was seen that eddy shocklets could reduce turbulent mixing through both the production of counter fluctuating vorticity and the reduction of turbulence scale. The authors stated that the mechanism for these effects resulted from the instantaneous inviscid pressure field

6

induced about the front of the eddy. The authors further noted that the induced pressure field would always counter the initial vortex circulation over a portion of its contour, and for long enough times and weak enough eddies, the formation of counter vorticity and consequent eddy splitting would occur, resulting in a significant alteration of the mixing-layer structure.

Many, if not all, of the important features described above for nonreacting subsonic and supersonic mixing layers also occurred in reacting layers. A majority of the studies on reacting mixing layers were carried out at subsonic rather than supersonic speeds, however. Yule, Chigier, and Thompson [11] found that, consistent with nonreacting flow, many combusting flows contained coherent burning structures that interacted as they were convected downstream. They termed the burning region associated and moving with an eddy a "flamelet" and found that the flamelet formed in only part of an eddy. They found a range of eddy types existed in a diffusion flame (that occurred in a nonpremixed reacting mixing layer). Initially there existed unstable laminar flow that contained an unstable laminar diffusion flame. That region was followed by one containing sheets of vortex rings with smooth tongues of flame at the interfaces between the vortices and unburned reactants. This region was followed by a zone of other orderly vortex structures, including helical vortices, which also produced relatively smooth tongues of flame. This zone contained the characteristics of transition observed in nonreacting flow. Here, viscous forces have a stabilizing influence on the flow. As the viscous forces became less important and inertial forces predominately further downstream, the authors found that the orderliness of the eddies decreased and the flow became increasingly unstable and three-dimensional. With the introduction of three-dimensional effects, randomly moving cell-like flamelets also appeared. Even further downstream, this process evolved into a fully turbulent flow with eddies containing coherent ragged regions of burning, forming islands that were completely separated from the main flame. Yule et. al. [11] also examined the structure of a single eddy containing a flamelet in a simple gas diffusion flame. The basic structure of a tran-

sitional eddy before it interacted with other eddies is given in figure 1, which was taken from reference [11]. The eddy contained separate regions of fuel and air that rolled up into the vortex, as well as a viscous core containing a mixture of fuel, oxidants, and products. A flame existed along the interface region where large transverse gradients of temperature and species concentration occurred. The local thickness of this region depended on the residence time and strength of the vortex, the local diffusion coefficients, and chemical kinetics. The molecular mixing required before fuel and air react was enhanced in the eddy by stretching of the fuel/air interface due to the vorticity that the eddy contained. Preheating of fuel and air then took place primarily along the interface zone where mixing was taking place on a molecular scale. Combustion then occurred in the interface at or near stoichiometric conditions. During these processes, the vortex continued to convect downstream, and the induced velocity within the eddy due to its vorticity continued to produce valleys and an increase in vortex dimensions. This eddy growth resulted in further entrainment of fuel and air, producing flame and mixing layer growth.

Yule et. al. [11] then went on to discuss the evolution of turbulent eddies from transitional eddies. The structure is pictured in figure 2, again taken from reference [11]. The eddy has now taken on a three-dimensional structure, and it has begun to lose the circumferential coherence about its associated flamelet. Additionally, there now existed an irregular vorticity distribution within the eddy, which was interpreted to be due to the presence of smaller eddy scales now existing within the main eddy. Mixing down to molecular levels was still produced by vortical stretching, and the process appeared, in fact, to be more pronounced in the turbulent eddy. In addition, the irregularity of the structure also produced a range of flamelet structures, resulting in a "ragged" flame front trailing the eddy. The authors concluded their study of large coherent structures in reacting flow by noting that such structures could lead to overall reduced combustion efficiency because of unmixedness. Unmixedness occurred when fuel and air could not effectively mix because each gas was bound up in vortical structures during its passage through a combustion

region. They did suggest that large eddies could be broken up by increasing the shear stresses in the flow in regions of steep velocity gradient or by the imposition of swirl into the flow.

Masutani and Bowman [12] also studied the structure of a chemically reacting plane mixing layer. They examined the reaction in the mixing layer between a stream of dilute nitrous oxide and a stream of dilute ozone and observed similar behavior to that seen by the previous authors. They found that the mixing layer had three streamwise states. First, there existed fingers of unmixed free-stream fluid that sometimes reached entirely across the layer. Next, there appeared a region of mixed fluid in a finite-thickness interfacial diffusion zone that bordered parcels of unmixed fluid. Finally, the layer consisted of regions of mixed fluid or nearly homogeneous composition in a global sense.

Keller and Daily [13] conducted an experimental study of a gaseous, two-stream, reacting mixing layer flow fueled by propane, with one stream made of hot combustion products and the other stream containing cold unburnt reactants. They found that the mixing layer structure was qualitatively unaffected by heat release for the range of conditions that they studied. Mungal, Dimotakis, and Hermanson [14] experimentally studied the reacting mixing layer created between a dilute hydrogen stream and a dilute fluorine stream over a wide range of conditions. They also observed the presence of large hot coherent structures in the layer that strongly influenced the mixing and entrainment of fuel and oxidant and the overall structure of the flow field.

Hermanson, Mungal, and Dimotakis [15] extended the work described in reference [14], but with significantly higher heat release. They found that at the higher temperature resulting in this case, the flow still appeared to be dominated by large-scale structures that were separated by cold tongues of fluid that extended well into the layer. Thus, the structure did not appear to be altered by heat release and continued to be predominatly two-dimensional. They also found that with significant heating and the resulting large density changes, the shear layer thickness did not increase, and in fact showed a slight

decrease. This reduction in layer thickness with increasing heat release was further confirmed by the resulting velocity profiles that showed noticeably higher values of transverse velocity gradient with increased heating. The authors then went further to note that since the layer width did not increase with temperature, and since the density of the layer was substantially reduced by heating, the volumetric entrainment rate of free-stream fluid into the layer must also be greatly reduced by heat release. Pitz and Daily [16] carried out an experiment to study a turbulent propane-air mixing layer downstream of a rearward facing step. They also found that large-scale structures dominated the flow and that the growth of these eddies influenced the reaction zone. Reaction took place mainly in the eddies, although the eddies were not confined to the velocity gradient region of the layer. Therefore, the resulting flame spread faster into the premixed reactants than did the mixing layer defined by the mean velocity. Thus the region of the mixing layer defined by the velocity gradient did not coincide with the region of high chemical reaction and heat transfer. Broadwell and Dimotakis [17] surveyed a number of recent papers describing experiments of reacting mixing layers. Based on these papers and their experience, they then discussed the implications for modeling such flows. Their three principal conclusions were that molecular transport retained a significant role in turbulent mixing phenomena, even when the flow was fully developed; large-scale structures controlled entrainment, which then provided conditions for the subsequent mixing processes; and mixing layers remained unsteady at the largest temporal and spatial scales.

Reacting mixing layer studies using analytical or numerical approaches have also been carried out. Carrier, Fendell, and Marble [18] used a singular perturbation technique to modify their Burke-Schumann thin flame solution for a more realistic finite thickness reaction zone in a mixing layer. They studied the effect of fluid strain on the flame; their strain increased the interfacial exposure of fuel and oxidant, and convected additional reactant into the flame. Riley and Metcalfe [19] directly simulated a subsonic, temporally developing and reacting mixing layer by using a pseudospectral numerical method and

10

a binary single-step irreversible reaction with no heat release. Using the approach, they were able to consider the effect of the turbulence field on chemical reaction. Their results were shown to be consistent with similarity theory and in approximate agreement with experimental data. McMurtry, Jou, Riley, and Metcalfe [20] extended the preceding work to consider the effect of chemical heat release on a subsonic, temporally developing mixing layer. They solved both the compressible form of the governing equations as well as a more computationally efficient form of the equations valid for low Mach numbers. Reaction was again modeled with a binary, single-step, irreversible reaction. The authors found with their simulations that the thickness of the mixing layer and the amount of mass entrained into the layer decreased when the heat release rate due to exothermic reaction was increased. Likewise, the resulting product formation also decreased as the heat release rate increased.

Menon, Anderson, and Pai [21] studied the stability of a laminar, premixed, spatially developing, supersonic mixing layer undergoing chemical reaction. They introduced an infinitesimal disturbance into the layer and examined its spatial stability for both reacting and nonreacting flows. Chemical reaction was shown to have a significant effect on flow stability. The authors found that with reaction, the disturbance amplification rate was higher and the wave speed lower as compared with nonreactive cases. Also, the free-stream Mach number was shown to have little effect on stability when the flow was reacting.

In this study, a numerical model has been developed for describing general two- or three-dimensional, high subsonic or supersonic, chemically reacting flows. This model was then adapted to a supersonic, chemically reacting mixing layer. Reaction in many practical devices takes place in mixing layers, so that the problem chosen, while being geometrically simple, still retained the fluid mechanical and chemical complexities that were under consideration. Computer programs have been developed that numerically solve the governing equations resulting from the model. The programs used either a hybrid MacCormack-Householder technique [22] or a family of high-order compact finite difference

11

techniques developed by Carpenter [23] to solve the Navier-Stokes and species continuity equations that describe multiple species undergoing chemical reaction. Momentum, heat, and mass diffusion were defined with a multicomponent finite-rate scheme; and a real gas thermodynamics model was employed.

Using the computer programs developed in this work, detailed studies of the supersonic, spatially developing and reacting mixing layer were undertaken. Because of their importance in subsonic layers, consideration was given first to the existence of vortical structures in a supersonic reacting mixing layer. The effects of such structures on the development of the layer were then explored and compared with the literature cited earlier. Particular emphasis was given in this study to the mixing of fuel and oxidant in the layer, the resulting chemical reaction, the effect of chemical heat release on mixing, and the existence of supersonic unmixedness. The existence of unmixedness next lead to a study of fuel-air mixing enhancement to improve the degree of chemical reaction that could be achieved in a mixing layer. Findings from this study were finally applied to actual scramjet engine configurations. The overall combustion efficiency of these configurations was significantly improved using the new techniques.

Before beginning our analysis of the spatially developing and reacting mixing layer, it is appropriate to review the theory and numerical methods upon which the analysis is based. They are discussed in the following section.

Theory

Governing Equations

The Navier-Stokes, energy, and species continuity equations governing multiple species undergoing chemical reaction have been derived by Williams [24]. The terms used in these and subsequent equations are defined in the appendix at the end of this chapter. The governing equations are given by

12

Continuity

$$\frac{\partial \rho}{\partial t} + \nabla \cdot (\rho \vec{V}) = 0 \tag{1}$$

Momentum

$$\frac{\partial(\rho \vec{V})}{\partial t} + \nabla \cdot (\rho \vec{V} \vec{V}) = \nabla \cdot \tau + \rho \sum_{i=1}^{ns} f_i \vec{b}_i \tag{2}$$

Energy

$$\frac{\partial(\rho E)}{\partial t} + \nabla \cdot (\rho \vec{V} E) = \nabla \cdot (\tau \cdot \vec{V}) - \nabla \cdot \vec{q} + \rho \sum_{i=1}^{ns} f_i \vec{b}_i (\vec{V} + \tilde{V}_i) \tag{3}$$

Species Continuity

$$\frac{\partial(\rho f_i)}{\partial t} + \nabla \cdot (\rho \vec{V} f_i) = \dot{w}_i - \nabla \cdot (\rho f_i \tilde{V}_i) \tag{4}$$

where

$$\tau \equiv \tau_{ij} = -\delta_{ij} p + \mu \left(\frac{\partial u_i}{\partial x_j} + \frac{\partial u_j}{\partial x_i} \right) + \delta_{ij} \lambda \frac{\partial u_k}{\partial x_k} \tag{5}$$

and

$$\vec{q} = -k \nabla T + \rho \sum_{i=1}^{ns} h_i f_i \tilde{V}_i + R^\circ T \sum_{i=1}^{ns} \sum_{j=1}^{ns} \left(\frac{X_j D_{T_i}}{M_i D_{ij}} \right) (\tilde{V}_i - \tilde{V}_j) \tag{6}$$

Radiation heat transfer is not included in equation (6). Also,

$$E = \sum_{i=1}^{ns} h_i f_i - \frac{p}{\rho} + \sum_{i=1}^{3} \frac{u_i^2}{2} \tag{7}$$

$$h_i = h_i^\circ + \int_{T_r}^{T} c_{p_i} dT \qquad i = 1, 2, ..., ns \tag{8}$$

$$p = \rho R^\circ T \sum_{i=1}^{ns} \frac{f_i}{M_i} \tag{9}$$

The diffusion velocities are found by solving

$$\nabla X_i = \sum_{j=1}^{ns} \frac{X_i X_j}{D_{ij}} (\tilde{V}_j - \tilde{V}_i) + (f_i - X_i) \frac{\nabla p}{p} + \frac{\rho}{p} \sum_{j=1}^{ns} f_i f_j (\vec{b}_i - \vec{b}_j) +$$
$$\sum_{j=1}^{ns} \frac{X_i X_j}{\rho D_{ij}} \left(\frac{D_{Tj}}{f_j} - \frac{D_{Ti}}{f_i} \right) \frac{\nabla T}{T} \tag{10}$$

13

Note that if there are ns chemical species, then $i = 1, 2, ..., (ns-1)$ and $(ns-1)$ equations must be solved for the species f_i. The final species mass fraction f_{ns} can then be found by conservation of mass since $\sum_{i=1}^{ns} f_i = 1$.

Thermodynamics Model

To calculate the required thermodynamic quantities, the specific heat for each species is first defined by a fourth-order polynomial in temperature

$$\frac{c_{p_i}}{R} = A_i + B_i T + C_i T^2 + D_i T^3 + E_i T^4 \tag{11}$$

The coefficients are found by a curve fit of the data tabulated in reference [25]. Knowing the specific heat of each species, the enthalpy of each species is then found from equation

To determine the equilibrium constant (required in the next section) for each chemical reaction being considered, the Gibbs energy of each species must first be found. For a constant pressure process, $\frac{c_p}{T}$ from equation (11) is first integrated over temperature to define the entropy of the species, and then the resulting expression is integrated again over temperature to obtain a fifth-order polynomial in temperature for the Gibbs energy of each species.

$$\frac{g_i}{R} = A_i(T - T \ln T) + \frac{B_i}{2}T^2 + \frac{C_i}{6}T^3 + \frac{D_i}{12}T^4 + \frac{E_i}{20}T^5 + F_i - G_i T \tag{12}$$

The coefficients F_i and G_i are again defined in reference as the difference between the Gibbs energy of product and reactant species.

$$\Delta G_{R_j} = \sum_{i=1}^{ns} \gamma_{ji}'' g_i - \sum_{i=1}^{ns} \gamma_{ji}' g_i \qquad j = 1, 2, ..., nr \tag{13}$$

The equilibrium constant for each reaction can then be found from

$$K_{eq_j} = \left(\frac{1}{R^o T}\right)^{\Delta n} \exp\left(\frac{-\Delta G_{R_j}}{R^o T}\right) \tag{14}$$

where Δn is the change in the number of moles when going from reactants to products.

14

Chemistry Models

The rate of chemical reactions is often defined by using the Arrhenius Law. A modified form of of the Arrhenius law is usually employed when modeling supersonic combustion. It is given by

$$K_{f_j} = A_j T^{N_j} \exp\left(\frac{-E_j}{R^\circ T}\right) \tag{15}$$

The values of the preexponential constant A, power constant N, and the activation energy E have been determined for a number of reaction schemes. Unfortunately, there is a great deal of uncertainty for many chemical reactions. One of the best understood mechanisms, however, is the hydrogen-air reaction system. This is not the reason that hydrogen fuel was chosen for several scramjet concepts, but it has proven convenient for its combustor analysists! Values for A, N, and E for a typical hydrogen-air mechanism are given in Table 1. Knowing the forward rate, the reverse rate is then given by

$$K_{b_j} = \frac{K_{f_j}}{K_{eq_j}} \tag{16}$$

Once the forward and reverse reaction rates have been determined, the production rates of the species are found from the law of mass action. For the general chemical reaction

$$\sum_{i=1}^{ns} \gamma'_{ji} C_i \overset{K_{f_j}}{\rightleftharpoons} \sum_{i=1}^{ns} \gamma''_{ji} C_i \qquad j = 1, 2, ..., nr \tag{17}$$
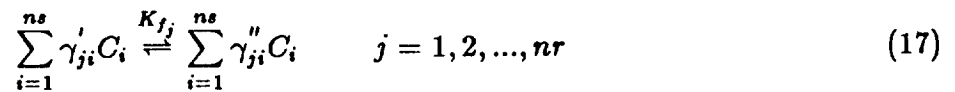
the law of mass action states that the rate of change of concentration of species i by reaction j is given by [24]

$$(\dot{C}_i)_j = (\gamma''_{ji} - \gamma'_{ji})[K_{f_j} \prod_{i=1}^{ns} C_i^{\gamma'_{ji}} - K_{b_j} \prod_{i=1}^{ns} C_i^{\gamma''_{ji}}] \qquad i = 1, 2, ..., ns \tag{18}$$

The net rate of change in concentration of species i by reaction j is then found by summing the contributions from each reaction

$$\dot{C}_i = \sum_{j=1}^{nr} (\dot{C}_i)_j \tag{19}$$

15

Finally, the production of species i can be found by multiplying its rate of change of concentration by its molecular weight.

$$\dot{w}_i = \dot{C}_i M_i \tag{20}$$

The source terms in equation (4) are now determined as a function of the dependent variables.

Molecular Diffusion Models

The coefficients governing the molecular diffusion of momentum, energy, and mass are determined from models based on kinetic theory. The set of models that is often used is now described. Individual species viscosities are computed from Sutherland's law

$$\frac{\mu}{\mu_o} = \left(\frac{T}{T_o}\right)^{1.5} \frac{T_o + S}{T + S} \tag{21}$$

where μ_o and T_o are reference values and S is Sutherland's constant. These constants are tabulated for many species in references determined, the mixture viscosity is found from Wilke's law

$$\mu_m = \sum_{i=1}^{ns} \frac{\mu_i}{1 + \frac{1}{X_i}\sum_{j=1,j\neq i}^{ns} X_j \phi_{ij}} \tag{22}$$

where

$$\phi_{ij} = \frac{[1 + (\frac{\mu_i}{\mu_j}\frac{\rho_j}{\rho_i})^{0.5}(\frac{M_i}{M_j})^{0.25}]^2}{\frac{4}{\sqrt{2}}(1 + \frac{M_i}{M_j})^{0.5}} \tag{23}$$

Species thermal conductivities are also computed from Sutherlands's law

$$\frac{k}{k_o} = \left(\frac{T}{T_o'}\right)^{1.5} \frac{T_o + S'}{T + S'} \tag{24}$$

with different values of the reference values k_o and T_o' and the Sutherland's constant S'. These values are also tabulated for a number of species in references [27,28]. The mixture

thermal conductivity is computed using conductivity values for the individual species and Wassilewa's formula [30]

$$k_m = \sum_{i=1}^{ns} \frac{k_i}{1 + \frac{1}{X_i} \sum_{j=1, j \neq i}^{ns} X_j \phi'_{ij}} \tag{25}$$

where $\phi'_{ij} = 1.065 \, \phi_{ij}$ and ϕ_{ij} is taken from equation (18).

For dilute gases, Chapman and Cowling used kinetic theory to derive the following expression for the binary diffusion coefficient D_{ij} between species i and j [27].

$$D_{ij} = \frac{0.001858 T^{1.5} \left(\frac{M_i + M_j}{M_i M_j}\right)^{0.5}}{p \sigma_{ij}^2 \Omega_D} \tag{26}$$

Here, the diffusion collision integral Ω_D is approximated by

$$\Omega_D = \bar{T}^{-0.145} + (\bar{T} + 0.5)^{-2} \tag{27}$$

where $\bar{T} = \frac{T}{T_{\epsilon_{ij}}}$. Values of the effective temperature T_ϵ and the effective collision diameter σ are taken to be averages of the separate molecular properties of each species, giving

$$\sigma_{ij} = 0.5(\sigma_i + \sigma_j) \tag{28}$$

and

$$T_{\epsilon_{ij}} = (T_{\epsilon_i} T_{\epsilon_j})^{0.5} \tag{29}$$

For most molecules, the thermal diffusion coefficient is generally small when compared with the binary diffusion coefficient, and therefore, the thermal diffusion coefficient can be neglected. This is a fortunate fact, since values of the thermal diffusion coefficient are generally not known for most species. For low molecular weight molecules such as hydrogen, though, the thermal diffusion coefficient can be important. A set of relationships for the thermal diffusion coefficient of species having a molecular weight less than 5 has been developed by Kee et al. [31]. The reader is referred to reference [31] for further information and some numerical details for computing thermal diffusion coefficients of light molecules.

Once the binary and thermal diffusion coefficients for all species combinations are known, the diffusion velocities of each species can be computed from equation (10). The diffusion velocity is the velocity induced upon each species by all diffusion processes that are present in the flow. The solution of equation (10) requires solving a simultaneous equation system, with the number of equations equivalent to the number of species present for each component of the diffusion velocity. It should be noted that for i species, however, the system of i equations defined by (10) is not linearly independent. One of the equations must be replaced by the constraint $\sum_{i=1}^{ns} \rho f_i \tilde{V}_i = 0$ to make the system linearly independent. The resulting simultaneous system of equations must then be solved for the diffusion velocities.

The process of solving for the diffusion velocities can be computationally quite expensive. A coupled system of equations must be solved for each of the three components of the diffusion velocity at each computational grid point. This process can require as much time as solving the Navier-Stokes equations for the three components of the convection velocities. Alternately, for hydrogen-air chemistry where large amounts of nitrogen are present, it is sometimes assumed that each species is present as a "trace" in a mixture with N_2 N_2 with that process defined by its binary diffusion coefficient with N_2. Finally, for engineering calculations, it is often further assumed that the diffusivities of each chemical species present in the flow are the same. Then the diffusion of each species into the remaining species varies only with its respective concentration gradient. The diffusion velocities then decouple, and equation

$$\tilde{V}_{i,j} = - \frac{D}{f_i} \frac{\partial f_i}{\partial x_j} \tag{30}$$

where $\tilde{V}_{i,j}$ is the diffusion velocity vector of the i th species in the j th coordinate direction ($j = [x,y,z]$) and D is the binary diffusion coefficient. If the binary diffusion with N_2 is not used, the value of D is determined by chosing an appropriate value of the Schmidt number Sc since $D = \frac{\mu}{\rho Sc}$. The mixture viscosity μ is determined as before from Wilke's law. When the binary diffusion assumption is invoked, it is often further assumed that the mixture thermal conductivity can be defined by $k = \frac{C_p \mu}{Pr}$ after an appropriate value of the

18

Prandtl number Pr has been chosen.

Turbulent Diffusion Models

While the techniques for defining the molecular diffusion of momentum, heat, and mass are reasonably well established in a supersonic reacting flow, the same statement cannot be made for our ability to describe the turbulent diffusion of these quantities. Work to develop methods for modeling turbulent supersonic combustion is now in its early stages. Conventional approaches, that are employed in the calculations that follow, have included the use of algebraic eddy viscosity models or differential transport models. Several eddy viscosity models have been used, in particular the Cebeci-Smith model [33] and the Baldwin-Lomax model [34]. The differential transport models include the k/ϵ turbulent kinetic energy model and its variants [35], a modified k/ϵ model that included a supersonic flow compressibility correction [36,38], and a multiple dissipation length scale (k/multiple ϵ) model with a compressibility correction [36,37] that addressed the existence of multiple dissipation length scales that exist in the energy cascade of a turbulent flow. In addition to these differential transport models, the algebraic Reynolds stress models of Rodi [39] and Sindir [40] have also been considered for use in modeling turbulent supersonic reacting flows. A review of all of these models has been given by Sindir [40]. In that review, he also critically compared the models against several nonreacting flow experiments prior to using the models for studying flows with reaction. He concluded that forms of the algebraic Reynolds stress model that he considered produced the best agreement with nonreacting data. He also found that the multiple dissipation length scale model did not offer any advantage over the basic k/ϵ model.

All of the turbulence models described above have a major disadvantage when applied to reacting flow fields: they fail to account for the important coupling between the fluid mechanics and the chemistry. Turbulent fluctuations in the fluid mechanic variables have a direct effect upon the species production rates. The coupling between these two fields

occurs through the Arrhenius rate expression, equation The Reynolds averaging process applied to the governing equations eliminates the direct effect of temperature and species fluctuations on species production rates. For example, a positive temperature fluctuation would cause a decrease in the size of the exponential argument of the Arrhenius rate expression, with a corresponding increase in the forward kinetic rate of a particular reaction. This would in turn produce an increase in the time rate of change of the products of that reaction. More importantly, if the reaction were at a critical point, where perhaps a small increase in temperature would cause a reaction to enter an ignition stage, the entire species distribution of the flow field downstream could be changed.

Two promising ways for accounting for the effects of fluid and species fluctuations on chemical reaction would be through probability density functions or direct numerical simulation. The application of the probability density function approach to a reacting flow has been covered by Stephen Pope in a recent book published by the American Institute of Astronautics and Aeronautics [41] so this subject will not be further addressed here. Direct numerical simulation offers another attractive approach for modeling a turbulent reacting flow. The method has been used for a several years to accurately model lower speed reacting flows [42,19,43]. With this approach, the Navier-Stokes and species continuity equations are resolved down to the smallest scale features of the flow field. The size of those scales goes inversely with the Reynolds number of the flow field. Clearly, for the high Reynolds numbers that occur in typical supersonic reacting flows, the smallest scales can become quite small, nessitating a very fine computational grid to resolve them. Also, when high speed flow undergoes chemical reaction, additional scales are introduced by the combustion process. Herein lies the principal difficulty of applying direct simulation to a high speed flow. The difficulty is not so much one of numerical algorithms as it is of computer power. Highly accurate numerical algorithms are required, but appropriate high-order finite-difference methods, finite-volume methods, or spectral methods have been developed that satisfy that requirement. The large number of computational grid points required

to resolve the smallest scales in the flow requires large computer storage, and therefore, meaningful calculations can be carried out only on large memory machines. Currently, direct numerical simulations have been made for nonreacting flows with Reynolds numbers up to about 10000 on a Cray 2 computer chemically reacting flow of a similar Reynolds number.

As an alternative to direct numerical simulation with its intensive memory requirements, it is possible to model rather than compute the smallest scales. In this approach, termed large eddy simulation, the larger scales above a chosen wavelength are still computed. The smaller scales below the cutoff wavelength are modeled, however, using a subgrid scale model. Large eddy simulation is an attractive alternative because only the larger scale effects are computed, lessening the computer memory requirements for higher Reynolds number flows. Subgrid scale models must be constructed, though, that give an accurate rendering of the physics of small scale phenomena. This is a difficult task. Work is underway to develop subgrid scale models for nonreacting flow, for example the early work of Schumann for modeling high speed reacting flows. Little has been done so far with this technique, but it warrants serious attention in the future.

Discretization of the Governing Equations

Once the governing equations and required modeling are in hand, the equations can be discretized and integrated in space and time. We begin this process by expressing the governing equations (1) in vector form. In that form they become,

$$\frac{\partial \mathbf{U}}{\partial t} + \frac{\partial \mathbf{E}}{\partial x} + \frac{\partial \mathbf{F}}{\partial y} + \frac{\partial \mathbf{G}}{\partial z} = \mathbf{H} \tag{31}$$

where $\mathbf{U}$ is the vector of dependent variables, $\mathbf{E}, \mathbf{F}$, and $\mathbf{G}$ are flux vectors continuing convective and diffusive terms, and $\mathbf{H}$ is the source term containing body forces and the chemistry production terms. The temporally discrete form of equation (31) can then be

written as

$$\mathbf{U}^{n+1} = \mathbf{U}^n - \Delta t[\frac{\partial \mathbf{E}^n}{\partial x} + \frac{\partial \mathbf{F}^n}{\partial y} + \frac{\partial \mathbf{G}^n}{\partial z} - \mathbf{H}^{n+1}] \tag{32}$$

where n is the old time level and $n + 1$ is the new time level. The flux terms are written at the old time level in this study because the equations are advanced in real time at the smallest fluid time scale. As an option, the chemical source term is written implicitly [47,48] to allow for stiffness in the governing equations when chemistry time scales become small as compared to fluid time scales early in a calculation or when the system approaches chemical equilibrium. Otherwise, solution times would become prohibitively long.

Once the temporal discretization of equation (32) is established, the spatial derivatives must also be discretized. The earliest work employed the MacCormack-Householder scheme. In this approach, the unsplit, spatially second order MacCormack finite difference scheme [49] was used along with the Householder matrix solver [50] required to solve the block diagonal matrix resulting from the implicit source terms. Details of the method are given in reference [22].

To achieve a higher level of numerical accuracy, several high-order accurate methods were introduced into the computer codes by Carpenter. These included the spatially fourth-order accurate method of Gottlieb and Turkel [51], and the spatially fourth-order accurate compact scheme of Abarbanel [52] written for the Euler equations and generalized for the Navier-Stokes equations by Carpenter [23]. In addition, Carpenter further generalized the compact algorithm to include a family of schemes, each of which offered advantages relative to the particular problem being considered. Each algorithm was arrived at with appropriate combinations of Taylor series of a function in three dimensions. The tedious algebra that was required usually necessitated the use of a symbolic manipulator such as MAXIMA to generate the difference formula. These algorithms and further information for deriving them are discussed in more detail in reference [53].

Mixing Layer Results

Following the development of the theory and solution procedure described above, the combustion code was checked by comparison with a standard test case, the known solution for a spatially developing mixing layer. Lock [27] solved the incompressible boundary-layer equations for a laminar mixing layer with upper stream velocity U_1 and lower stream velocity U_2. The configuration is shown in figure 3 along with his solution for air with a velocity ratio $U_2/U_1 = 0.5$. The solution is similar and is plotted in terms of a similarity variable η versus the nondimensional streamwise velocity u/U_1. The definition of y was modified using the Howarth-Dorodnitzyn transformation

$$y = \int_0^y \frac{\rho}{\rho_e} dy \tag{33}$$

to allow comparison with the solution to the same problem based on the compressible Navier-Stokes equations. In equation(33), y is the transverse coordinate, and ρ and ρ_e are the field and edge densities, respectively. The definition for η reduces for incompressible flow to that used by Lock. Results from the computation for $U_2/U_1 = 0.5$ are also shown in figure 3. The calculations were made on a computational grid with 51 nodes in the streamwise direction, 51 nodes in the spanwise direction, and 51 nodes in the transverse direction across the layer. The grid was highly compressed in the transverse direction with a minimum grid spacing of 0.1 mm. The results become similar at a value of x/L equal to or greater than 0.1, where x is the streamwise coordinate and L is the streamwise length of the physical domain. The comparison of the computation with the exact solution of Lock is excellent for all values of η. The transformation coordinate η is highly stretched relative to the physical coordinate y. It is therefore clear from the comparison that the large velocity gradient across the mixing layer is well resolved by the chosen grid. Other validation cases for the code can be found in the literature [22,54,23,53,68].

Following checkout of the program with several test cases, the chemically reacting flow field in a non-premixed laminar, supersonic, spatially developing mixing layer was simulated with the code using both the second order and fourth order algorithms. The case that was chosen involved a hydrogen-air mixing layer initially separated by a finite

thickness splitter plate. The configuration is described schematically in figure 4. The overall domain is 5 cm high and 5 cm long. The height chosen places the boundaries well into the free stream, and the length allows initial development of the mixing layer. Initially, hydrogen fuel and air are separated by a 0.5 cm long splitter plate that is 0.02 cm thick and centered at $y = 2.5$ cm. Downstream of the plate, the fuel and air mix and ignition occurs at some further distance downstream of the plate base. From that point, chemical reaction between the fuel and air takes place. For the problem being considered, cold gaseous hydrogen is introduced above the plate at Mach 1.5, a Reynolds number of 3700 based on plate thickness, a temperature of 293 K, and a pressure of 0.101 MPa (1 atm). Hot air is introduced below the plate at Mach 1.5, a Reynolds number of 731, a temperature of 2000 K, and a pressure of 0.101 MPa. These conditions result in an initial hydrogen velocity of 1953 m/s and an air velocity of 1297 m/s; this yields a hydrogen-to-air velocity ratio of 1.5.

By using the configuration and conditions described above, the mixing-layer flow field is marched in time from the specified initial conditions to the conditions existing at 0.1 ms. The solution is obtained on a spatial grid with 219 nodes in the streamwise direction and 51 nodes in the transverse direction. The grid is compressed in x near the trailing edge of the plate and highly compressed in y in the region of the mixing layer, using a distribution identical to that used in the validation case described earlier. The resulting flow field is described in figures 5 through 23, which give pictures of the flow at an instant in time. Figure 5 shows a velocity vector field plot of the flow close to and on either side of the splitter plate and the developing mixing layer downstream of the base of the splitter plate. (Velocity vectors are shown for only every four streamwise and transverse grid points in this region.) Expansions of both streams through Prandtl-Meyer fans can be observed at the trailing edge of the plate. The higher velocity hydrogen stream and the lower velocity airstream are apparent as is the wake flow downstream of the plate. The development of the mixing layer with streamwise distance can also be seen. Two regions of instability

are also apparent in figure 5. The first region lies just downstream of the splitter plate approximately 1.0 cm beyond the initial station. The second region lies well downstream at approximately 4.0 cm from inflow. The flow is relatively quiescent between these two regions. The first instability is associated with an unstable separation bubble on the trailing edge of the splitter plate separating hydrogen and air, and the second instability is a Kelvin-Helmholtz instability that occurs downstream in a mixing layer with a sufficient initial flow disturbance. The instabilities can also be seen in figure 6 which shows a plot at 0.1 ms of streamwise velocity versus streamwise coordinate at three constant transverse stations located well within the mixing layer.

To examine the effect of chemical heat release on the instabilities in the flow field, the identical calculation was repeated without chemical reaction. The resulting plot of streamwise velocity versus streamwise velocity at 0.1 ms is shown in figure 7. By comparing figures 6 and 7, it appears that the upstream disturbance is essentially unaffected, but chemical reaction is small and endothermic in that region. Well downstream, however, heat release is large and exothermic, and that heat release reduces the amplitude of the instability. This result is consistent with the findings of references [15] and [20] for subsonic flow, which showed mixing is retarded by heat addition in an unconfined flow.

Contour plots of velocity and static temperature in the streamwise direction along the mixing layer are shown in figures 8 and 9. By comparing these figures, it can be seen that the temperature profiles at each x-station are consistently broader than the streamwise velocity profiles. This result is consistent with the discussion and experimental observations described earlier from references [1] through structures are present in the mixing layer, and the existence and growth of these vortices influence the growth and reaction in the mixing layer. The vortical character can be seen in figure 10, which gives the vorticity distribution in the mixing layer. Chemical reaction takes place not only in the interior of the mixing layer, but also in the eddies on the edges of the layer. These eddies lie outside the high velocity gradient region of the layer as can be seen by comparing

25

figure 8 with figure 10. Therefore, the resulting flame spreads transversely faster into the unreacted species than did the mixing layer defined by the high velocity gradient zone. Thus, the region of the mixing layer defined by the velocity gradient is not as transversely wide as the flame zone defined by temperature gradient in the mixing layer, in agreement with reference [16].

Figures 11 through 17 show plots at seven streamwise stations (x = 0.51, 0.58, 1.0, 2.0, 3.0, 4.0, and 5.0 cm) of the major chemical species (H_2, O_2, and H_2O) and minor chemical species (OH, H, O, HO_2, and H_2O_2). Contour plots giving the two-dimensional distribution of the species are given in figures 18 through 23. Initially, at x = 0.51 cm (fig. 11(b)), fuel and air have just begun to mix, and no significant amount of water has yet formed. A very narrow band of hydrogen peroxide (H_2O_2) is present just above the splitter plate center, and a very small amount of hydroperoxyl (HO_2) lies just below that spike. At x = 0.58 cm (fig. 12), the hydrogen and oxygen profiles begin to broaden, but no water has yet appeared in the layer. The hydrogen peroxide spike is still the most predominant, and, while the profile has not broadened, the peak has increased. (Note the ordinate in fig. 12(b) has been rescaled.) A small amount of hydroperoxyl still lies below the hydrogen peroxide peak, and small amounts of atomic hydrogen (H) and atomic oxygen (O) have appeared there. At x = 1.0 cm, as described in figure 13, the hydrogen and oxygen profiles have developed, and a small amount of water (8 percent by mass) has been produced in a narrow profile below the splitter plate centerline. The H_2 and O_2 profiles are appropriately depressed in the region of the water peak. Noticeably increased profiles of H, O, and OH also appear at this station just below the splitter plate centerline (y = 2.5 cm). The O and OH profiles lies slightly below the water peak; this is consistent with the spatial distribution of reactant species. Small amounts of HO_2 and H_2O_2 still remain at and just above the plate centerline.

Figure 14 diagrams the species profiles at x = 2.0 cm. The H_2, O_2, and H_2O profiles have broadened significantly more at this station, and the water peak has risen to

approximately 23 percent by mass. The minor species profiles have also broadened significantly, with atomic oxygen peaking at 3.0 percent, hydroxyl peaking at 2.0 percent, and atomic hydrogen peaking at 0.8 percent, all by mass. Small amounts of hydroperoxyl and hydrogen peroxide are still present just above the splitter plate centerline. With further movement downstream at $x = 3.0$ and 4.0 cm (figs. 15 and 16), the major and minor species profiles continue to develop, increasing both in width and in peak values. There are distinct distortions in the H_2 profiles in both figures because of eddies being located on the upper edge of the mixing layer. There is also a general migration of each profile to lower values of y with increasing streamwise coordinate. The increase in product species along the lower edge of the mixing layer is a direct result of preferential burning in this region of the layer. The mixing layer is most nearly stoichiometric there, and the temperature reaches values that favor rapid ignition and combustion. At the last streamwise station given in figure 17, $x = 5.0$ cm, the major and minor species profiles broaden considerably further and shift to even small values of y. The noticeable increase in the rate of spread of the species profiles is associated with the second instability that is present in the mixing layer in this region and is consistent with transitioning to a turbulent state.

Two-dimensional contour plots of the species are given in figures 18 through 23. The resulting structure as the mixing layer develops, described previously in figures 11 through 17, can be clearly seen in these figures. The first and second regions of instability are apparent for each species that are shown. The more rapid transverse spread of each species in the latter third of the layer can also be seen. A quiescent region between the two instabilities also occurs for each species, as expected. Additionally, there is a general downward migration of each of the product species with increasing streamwise coordinate. The structure of the product species, typified by water, in the downstream region of the layer is also interesting. The vortical nature of the flow, seen earlier in figure 10, results in regions of unreacted hydrogen gas being captured by regions (or "folds") of product water. Once captured, the regions of hydrogen have difficulty mixing with oxygen so that they

can ultimately react. This phenomenon, often termed "unmixedness," reduces the overall level of reaction that can be achieved, and contributes to a reduction in the efficiency of combustion. Under these conditions, mixing enhancement is required to achieve an acceptable degree of mixing and combustion efficiency.

Mixing Enhancement

Significant research has recently been directed toward the optimization of the scramjet combustor, and in particular the efficiency of fuel-air mixing and reaction taking place in the engine. In the very high speed vehicle configurations currently being considered, achieving a high combustor efficiency becomes particularly difficult. With increasing combustor Mach number, the degree of fuel-air mixing that can be achieved through natural convective and diffusive processes is reduced, leading to an overall decrease in combustion efficiency and thrust.

Because of these difficulties, attention has now turned to the development of techniques for enhancing the rate of fuel-air mixing in the combustor. As discussed earlier in this chapter, Brown and Roshko layer decreased with increasing Mach number, exhibiting a factor of three decrease in spread rate as compared with an incompressible mixing layer with the same density ratio. They concluded that the reduced spread rate was primarily a function of compressibility. It was also noted earlier that Papamoschou and Roshko [9] observed that the spreading rate of compressible mixing layers was significantly reduced over that of incompressible layers. The reduction in mixing layer spreading rate by approximately a factor of three or four, was shown in their experiment to correlate well with increasing convective Mach number. The authors therefore concluded that the reduced spreading rate was attributable to a stabilizing effect of the convective Mach number. Ragab and Wu [55] analyzed the spatially developing supersonic mixing layer using linear spatial stability theory. They also found that the decreased spreading rate of the mixing layer correlated well with convective Mach number, and their predictions agreed well over

most of the Mach number range with the results of Papamoschou and Roshko. The work presented in references [5] through [55] thus showed through both experiment and theory the difficulty in achieving a high degree of mixing in unenhanced supersonic mixing layers.

Faced with this challenge, several authors have numerically examined potential techniques for enhancing the mixing rates in supersonic mixing layers. Guirguis, et al. [56] showed that the spreading rate of a confined mixing layer could be improved if the pressure of the two streams was different. Encouraged by this result, Guirguis [57] inserted a bluff body at the base of the splitter plate separating the two streams. The body produced an instability further upstream in the layer and resulted in a more rapid rate of spread. Kumar, Bushnell, and Hussaini [58] discussed a number of mixing problems that might exist in scramjet combustors. Several techniques for enhancing turbulence and mixing in combustor flow fields were suggested and one enhancement technique that employed an oscillating shock was studied numerically. In this case, a premixed stoichiometric hydrogen-air flow was processed through a spatially and temporally oscillating shock wave, and the resulting flow was studied with and without chemical reaction. The oscillating shock was shown to increase the level of turbulence in the flow field, and the degree of turbulence enhancement was seen to increase with a decreasing frequency of shock oscillation. Chemical reaction as defined by an equilibrium model was shown to have little effect relative to the nonreacting results. Drummond and Makunda [22] studied fuel-air mixing and reaction in a supersonic mixing layer and applied several techniques for enhancing mixing and combustion in the layer. They found that when the mixing layer, with its large gradients in velocity and species, was processed through a shock with strong curvature, vorticity was produced. The vorticity then interacted with the layer and significantly increased the degree of mixing and reaction. Based on the results of the study, an alternate fuel injector configuration that used interacting parallel and transverse fuel injectors was designed by the authors, and that configuration significantly increased the amount of fuel-air mixing and combustion over a given combustor length. This work will be reviewed later in this

section.

Experimental studies have also been carried out to evaluate mixing enhancement techniques. Menon [60] studied the interaction between a weak shock wave and a supersonic mixing layer. He found that significantly increased spreading of the shear layer occurred downstream of the shock-shear layer interaction region. King, Thomas, and Schetz [61] studied the enhancement of mixing through the interaction of parallel and transverse jets. They found that the mixing rate of the injectors could be significantly increased by the combined parallel and transverse injection as compared to parallel injection alone. Sullins, et al. [62] studied the shear layer between a Mach 2 to 3 air stream and a sonic air stream. They observed, using Schlieren photography and velocity profile measurements, a 60 percent increase in shear layer growth rate when the static pressure of the supersonic stream reached approximately 1.3 times that of the sonic stream. The observations of Sullins were therefore consistent with the numerical results of Guirguis.

In this section, we will apply the theory and computer program developed in the previous section of the chapter to several candidate mixing enhancement techniques. We will begin with a study of two-dimensional mixing layers and jets and examine several means for improving the extent of mixing and combustion in these flows. Based on the results of this study, an alternate fuel injector configuration will be numerically designed that significantly improves the amount of fuel-air mixing and combustion that can be achieved. We will then move ahead to three dimensions and model the flow field in a generic supersonic combustor. Those flow field results will indicate a less than acceptable degree of fuel-air mixing in the combustor. A new fuel injector configuration will again be designed to improve the level of mixing efficiency.

Mixing Enhancement of Mixing Layers and Jets

Once the computer code developed in this effort was validated for nonreacting flow, it was then applied to several reacting flow cases. The purpose of this study was to

assess several candidate configurations for enhancing fuel-air mixing and reaction in a mixing layer that would then lead to a better understanding for achieving improved mixing and combustion in the supersonic combustor of a scramjet engine. The first three cases involved a supersonic, spatially developing and chemically reacting mixing layer. The first of these cases, shown in figure 24, served as a benchmark calculation in that it contained no enhancement mechanism. Case 1 involved a mixing layer developing between a fuel stream and an air stream that were initially separated by an infinitely thin splitter plate. The fuel stream was made up of a mixture of ten percent hydrogen and ninety percent nitrogen introduced above the plate at a velocity of 2672 m/s, a static temperature of 2000 K, and a static pressure of 0.101 MPa (1 atm). Nitrogen gas was included to reduce the speed of sound of the fuel mixture. Air was introduced below the plate at a velocity of 1729 m/s, a static temperature of 2000 K, and a static pressure of 0.101 MPa. These conditions resulted in a Mach number of 2 for both streams. The physical domain considered in this case was 0.1 m long and 0.1 m high. The computational grid was identical to that used in the validation case that was described earlier. The simulation of this case was begun at t=0 with static conditions (u=0, v=0) in the flow domain. At this time fuel and air flows were initiated off of the trailing edge of the splitter plate (in a method analogous to opening two valves) at the conditions given above, and the gases then proceeded downstream. The mixing layer then evolved between the two gases in both space and time. The calculation was then advanced in a real time sense until an integration time of approximately 0.1 ms was reached. This time represented 14 computational sweeps of the flow field and allowed a periodic solution to develop. Chemical reaction of the hydrogen and air occured after a sufficient degree of mixing had occured. The chemical reaction in this case (and the next two cases) was modeled using the one step hydrogen-air model described in Table 2.

Computational results for Case 1 indicate that the mixing layer develops slowly in a smooth laminar fashion. A Kelvin-Helmholtz instability begins downstream at an x/L of approximately 0.8, but there is an insufficient length in the region of interest for the

instability to evolve significantly. The temperature also rises smoothly in the layer due to both viscous heating and chemical reaction. The instability is apparent downstream, and an increased amount of water production and an associated temperature rise to 2353 K result due to increased reaction in the vortical structures that evolve in this region. This can be seen clearly in figure 25 which gives a contour plot of water mass fraction in the layer. Water begins appearing at an x/L of about 0.1, then evolves at a slowly increasing rate until an x/L of 0.8 is reached, and the the rate increases somewhat in the instability reaching a peak value of 2.4 percent by mass. Even with the increased water production that occurs in the region of the instability, however, the overall degree of reaction is still quite limited in this case. This difficulty is compounded even further by the limited transverse spread of the layer in the y coordinate direction with increasing values of the streamwise coordinate x. The mixing layer must exhibit significantly more transverse spread within the limit of the streamwise coordinate if an acceptable level of mixing and combustion efficiency is to be achieved.

In an attempt to improve the level of mixing and reaction in the benchmark mixing layer case considered above, two mixing enhancement mechanisms were employed. The first approach (denoted as Case 2) is described in figure 26. Here, the mixing layer considered in Case 1 is processed through two shocks entering the flow domain from the upper and lower boundaries. Each shock is set at an angle of ten degrees by choosing appropriate boundary conditions along the upper and lower boundaries beyond the shock that are consistent with a ten degree shock in a Mach 2 flow of hydrogen/nitrogen and air, respectively. The two shocks then propagate from the upper and lower boundaries into the flow and across the mixing layer. Computational results show no marked enhancement in mixing layer spread rate due to the stationary shocks. The instability is slightly further upstream at $x/L = 0.7$, just behind the location of shock interaction with the layer. The amplitude of the instability is not increased, however, and the viscous region of the layer as defined by the velocity gradient is not thickened relative to the previous case. Temperatures reach a peak

value of 3178 K in the center of the layer near $x/L = 1.0$, but the increase is due primarly to the temperature rise through the shocks and some small increase in water production resulting from the higher temperature of the reactants. Even with this further increase in water production, giving peak values of about 6 percent by mass, the overall degree of reaction and the amount of product that is produced is still quite low. This can be seen by viewing the water contour plot in figure 27 which shows a layer thickness defined by water that is not any greater than that observed in the previous unenhanced case.

The second enhancement study, designated as Case 3, is described in figure 28. Conditions are again the same as in the previous two studies. In this case, a small square cylinder is placed along the fuel-air interface at $x/L = 0.2$. The body is 0.0012 m high and 0.002 m long. When the body is placed in the flow, it results in the formation of a bow shock just ahead of the body. The shock has strong curvature in the immediate neighborhood of the body. When the high velocity gradient region of the mixing layer is processed by this curved shock, vorticity is produced. The vorticity is then convected downstream where it produces enhanced macromixing of fuel and air. For this case, computational results indicate that the velocity field becomes unstable near the trailing edge of the interference body, and the thickness of the layer as defined by the velocity gradient grows rapidly with increasing streamwise coordinate. Rapid growth of the layer is also detected in the temperature distribution across the layer. A significant amount of vortical structure is also detected in the temperature field, and the individual vortices grow and amalgamate with one another as the layer develops with increasing streamwise distance. A peak temperature of 2500 K was observed at the center of several of the vortical structures. The water mass fraction also peaked at the centers with values as high as 3.4 percent by mass. The layer thickness defined by water mass fraction that is shown in figure 29 is significantly greater at all values of x relative to the previous two cases in this study.

While spread rate gives a good visual indication of the development of a mixing layer, a more useful and practical indication of mixing is given by the mixing efficiency of the layer.

33

The mixing efficiency is defined as a number between 0 and 1 that specifies the amount of fuel which could react at any x station if chemical reaction was taking place. Therefore, if all fuel could be consumed at a given x station, the mixing efficiency at that station would be unity. The mixing efficiency plotted as a function of the streamwise coordinate for Cases 1 through 3 is given in figure 30. The efficiency values for the three cases should be viewed in a relative sense because there are significant regions of fuel and air that can never mix since they are located at large transverse distances away from the mixing layer. What is important in this comparison, then, is the relative degree between the cases to which efficient mixing takes place. All three cases show a similar streamwise development of mixing efficiency to the 0.02 m station. Beyond that location, Cases 1 and 2 exhibit a similar slow development in efficiency, while Case 3 experiences a significant growth in mixing efficiency. The more rapid spread of the mixing layer due to the higher level of induced vorticity in case 3, that was observed in the earlier results, translates directly into a significantly higher level of mixing efficiency. Near the outflow station, the peak mixing efficiency of Case 3 is approximately four times that of Case 1 and three times that of Case 2. The oscillatory nature of the mixing efficiency plots for the three cases is related to the instantaneous structure present in each of the mixing layers at the time that the results are plotted. The structure of the plots can be directly tied to the representation of layers given in figures 25, 27, and 29. At that instant in time (0.1 ms), the highest rate of chemical reaction and the largest amount of product at a given x station is present in the neighborhood of the largest vortical structures, whereas less product is present at stations where the layer pinches between the vortices.

Once fuel and air have mixed, the degree to which they then react is defined at any streamwise station by the combustion efficiency. The combustion efficiency is again a number between 0 and 1 that defines the degree of chemical reaction that has taken place. The combustion efficiency that results for Cases 1 through 3 is given in figure 31. Comparison between the three cases should again be made in a relative sense due to the

34

geometry of the mixing layer. In addition, the one-step chemistry used to model reaction for Cases 1, 2, and 3 underestimates water production relative to the more complete model used later in this study. The model is still useful for this comparison, however. The combustion efficiency results given in figure 31 follow trends quite similar to those observed for mixing efficiencies given in figure 30. All three cases exhibit similar increases in combustion efficiency up to the 0.02 m station, but then Case 3 shows a significant increase over the other two cases. This trend continues until the 0.08 m station, where the combustion efficiency for Case 2 increases rapidly. Reexamination of the mixing efficiency for Case 2 shows, however, that this increase is not related to improved mixing, but rather to an increased reaction rate following a significant temperature rise through the shocks present in Case 2. Overall, combustion efficiencies for Case 3 are nearly 3 times higher than Case 1 and 1.5 times higher than Case 2. It is also important to note that the higher levels of mixing efficiency achieved in Case 3 occur well upstream in the layer relative to efficiency increases in the other two cases. Therefore, enhancement techniques of the type used in Case 3 may be an effective means of shortening the overall combustor length while still retaining a high degree of chemical reaction and the associated thrust.

To better understand the success of enhancement on fuel-air mixing, statistics of the resulting flow field in Case 3 were next examined. The results of the Case 1 benchmark analysis were also included in this study to allow comparison with Case 3. To extract these statistics from the simulations, values of the flow variables were collected at selected spatial locations over 50 time steps representing approximately two computational sweeps of the flow field. The resulting statistical features of the flow are summarized in Table 2. Included in the table are peak values of root mean square total velocity, streamwise velocity, temperature, density, and water mass fraction normalized by their respective mean values. Also included are peak values of the of the mean total velocity, the peak Reynolds stress normalized by the free stream dynamic pressure, and the layer vorticity thickness normalized by streamwise distance. In addition, a spectral analysis of the fluctuating

variables was also conducted. Results of the analysis were correlated in terms of a frequency nondimensionalized by the ratio of local velocity and local vorticity thickness. Significant energy was found to exist in the upstream fluctuating velocity field at frequencies of 0.01, 0.06, 0.09, and 0.12. Well downstream in the layer, the energy spectrum was quite broad, and there were no significant local peaks. This distribution indicated that the flow was transitioning, thus justifying the collection of statistical data. The tabulated values of vorticity thickness in Table 2 indicate that the mean growth rate is enhanced by about 40 percent in Case 3 as compared to Case 1. The fluctuating quantities also exhibit significantly higher values for Case 3. The Reynolds stress, and the fluctuating values of temperature, density, and water mass fraction are approximately twice as large in the enhanced case as compared to the unenhanced case, and the fluctuating total velocity is nearly four times as high. The statistical results, therefore, also indicate a significant improvement in mixing and combustion in Case 3.

The success achieved with the mixing enhancement technique employed in Case 3 motivated the authors to apply this approach to a more realistic configuration. The fuel injection strut of a conventional scramjet engine was chosen for study. The fuel injection struts provide locations for instream injection of gaseous hydrogen fuel into the air coming from the inlet of the engine. Fuel is injected in both a parallel and transverse direction to the incoming air stream. Transverse injection predominates over parallel injection when the engine is operating in the high Mach number regime to speed fuel-air mixing and combustion. At lower Mach numbers, more parallel injection is used to slow the mixing process and achieve a heat release schedule similar to that achieved at higher Mach number. A schematic of a typical injector configuration on the trailing edge of a fuel injection strut is given in figure 32. Transverse injection takes place following a rearward facing step that provides improved flameholding, and parallel injection occurs at the the strut base. The results achieved in Case 3 suggested that a reorentation of the injectors might improve the rate of fuel-air mixing and chemical reaction that could be achieved downstream of

the strut. That change is reflected in figure 33. In the new design, the parallel injector has been moved from the base of the strut to the vertical wall of the rearward facing step. The transverse injector now produces a curved bow shock that interacts with the high velocity gradient of the jet from the parallel injector resulting in vorticity production. The transverse jet thus serves a similar function to that provided by the interference body employed in Case 3. The present design is more practical, however. The solid interference body would produce significant losses in an engine, and aerodynamic heating would also pose a problem. The transverse injector is present in both strut designs, however, and so it introduces no significant losses in the new design as compared to the old one.

To assess the new strut design, a computational study was again performed. The calculation was begun at the rearward facing step. A parallel slot fuel injector was located on the face of the step that injected a mixture of ten percent hydrogen and ninety percent nitrogen gas at a velocity of 2672 m/s, a temperature of 2000 K, and a pressure of 0.101 MPa (1 atm). The injector was 0.064 cm high and located 0.032 cm above the strut wall. A transverse slot fuel injector was located 0.26 cm downstream of the step. An identical hydrogen-nitrogen mixture was injected there at 2672 m/s, a temperature of 2000 K, and a pressure of 0.505 MPa. The slot was sized to be one-fifth the width of the parallel jet so that the same amount of fuel was introduced from each injector. The strength of the transverse jet insured that it would produce a shock of sufficient strength to result in significant vorticity production.

With the new strut now configured, two cases were considered. The first case (identified as Case 4) considered operation of only the parallel injector. Case 5 involved operation of both the parallel and transverse injectors. Both cases were computed on a computational grid of 218 streamwise points and 51 transverse points. The grid was highly compressed in the transverse direction about the parallel injector and highly compressed in the stream-wise direction about the transverse injector. Chemistry was modeled in both cases using the nine species, eighteen reaction, hydrogen-air scheme described in Table 1. This model

37

provided a more realistic description of reaction than the one-step model, but it was more computationally expensive. However, it seemed more appropriate to apply the more detailed model to these practical cases to more accurately represent product production and heat release in the simulation. Computational results for this case show that the unenhanced parallel jet behaves much like the unenhanced mixing layer in Case 1. Velocities exhibit mild instability further upstream in this case, but there is no significant growth of the jet. Lack of growth is observed in the temperature distribution. The thermal layer is somewhat thicker than the velocity thickness due to burning, heat release, and a resulting temperature rise on the edges of the layer. A peak temperature of 2636 K is reached near the end of the jet. Water contours at 0.1 ms, that result from the complex reaction process, are shown in figure 34. The water contours show only a moderate degree of spread in the water field. Peak values of around 22 percent by mass of water are achieved near the end of the layer, however, indicating that a significant degree of chemical reaction does occur where fuel and air are able to sufficiently mix.

To improve the degree of fuel-air mixing, the transverse fuel injector was activated so that it might interact with the parallel injector. The degree of mixing enhancement induced when the parallel and transverse jets interact is significant. The interaction of the parallel jet with the curved bow shock ahead of the transverse jet again produces vorticity, resulting in increased mixing. The fuel jets develop more rapidly and there is a significant increase in the spread of the jet. A peak temperature of 2705 K is reached downstream in the reaction zone. The water contour plot in figure 35 shows markedly more jet development due to the interaction. The jet spreads much more rapidly than in the previous case and water mass fractions of as high as 24 percent occur across appreciable portions of the jet.

A more quantitative comparison of the last two cases is again made by examining their mixing and combustion efficiencies. A comparison of mixing efficiencies for Cases 4 and 5 is given in figure 36. The mixing efficiency of Case 5 increases much more rapidly than

38

Case 4 due to enhancement. Efficiencies of around 90 percent are achieved in only 40 percent of the solution domain length, whereas the unenhanced Case 4 requires 75 percent of the solution length to achieve the same level of mixing. This is especially noteworthy since twice as much fuel is being injected in Case 5 as compared to Case 4. Similar results are also observed when combustion efficiencies for the two cases are compared in figure 37. Combustion efficiencies of about 80 percent are obtained for the enhanced case within the first 40 percent of the solution length whereas the unenhanced case requires 75 percent of the solution length to achieve the same level of reaction. The higher combustion efficiencies that occur at earlier streamwise stations are again achieved with twice the amount of injected fuel. It is clear, then, that the simple enhancement technique employed in this study is quite effective in achieving a higher level of fuel-air mixing and combustion in shorter streamwise distances as compared to more conventional unenhanced approaches. The same or similar approaches should therefore offer an efficient means for achieving improved levels of combustion efficiency with a shorter overall combustor length.

Mixing Enhancement in Scramjet Engine Flow Fields

We will now move from two-dimensional to three-dimensional analyses and first examine simple non-reacting wall jets in supersonic flows in order to validate the codes and to gain an understanding of injection flow fields. We will then describe a numerical study of fuel-air mixing in a model generic supersonic combustor. Results from this study showed that the amount of fuel penetration and fuel-air mixing that could be achieved by the present design was limited below that required for acceptable combustor performance. To improve the degree of fuel-air mixing, two injector ramp enhancement configurations, developed in an experimental effort by Northam, Greenberg, and Byington [63], were chosen for study using numerical simulation. One of these configurations was shown to significantly improve the degree of fuel-air mixing, and appeared to be an excellent candidate for use in actual combustor configurations.

Fuel Injection Modeling

We will now consider the geometrically simple case of a circular (or oval) fuel jet issuing at an angle from a flat surface into a supersonic airstream. Although the geometry for such a problem might be simple to describe (see figure 38), the flow itself in the region of the injector is very complex and involves strong shocks and expansions, separation, vorticity generation, and possible reaction. A schematic for the flow in the injector near-field for a 90 degree (normal) wall jet is shown in figure 39. A bow shock is formed ahead of the jet with both separation ahead and behind the shock. In addition, a separated zone is seen behind the jet with the flow turning over the reattachment point generating a reattachment shock. The jet itself is rapidly turned by the air flow with initial penetration defined in general by the top of the Mach disk shown in the figure. An important phenomena in the jet-fluid interaction is the creation of strong counter-rotating vortices in the fluid as well as smaller jet core vortices. The influence of these vortices in mixing the fuel with the airstream can be significant. Such flows represent an important test of the ability of the computer code to adequately model scramjet combustor flow-fields.

Modeling injection flow fields requires a high number of points in the elliptic region of the jet where the full Navier-Stokes must be used. Hence, in order to faciliate rapid engineering calculation for regions away from the near-field of the injector, use has been made of a parabolized version of the three-dimensional computer code described earlier. This code was developed by Kamath [66] and allows marching solutions in regions of the flow which are steady and mainly supersonic. The computational stragegy for realistic computations for such flows is to use the marching (PNS) version of the code for upstream calculations (to approximately ten jet diameters upstream of the injector), perform a full elliptic solution in the region of the injector, and then to pass a steady inflow plane back to the marching code at about ten jet diameters downstream of the injector. The solution is then marched to the end of the domain.

The first case examined is that of sonic helium injection from from single orifices at angles of both 15 and 30 degrees from the wall surface. The experiments were conducted in Mach 3 air flow by Mays, Thomas and Schetz [65] and are describe in detail in that reference. The turbulence model used in this work was the Baldwin-Lomax algebraic model with a turbulent Schmidt number of 0.5. The rectangular grid in the elliptic (jet) region is 51 (axial) by 41 by 41. The grid was clustered at the jet centerline and at the jet axial location as well as at the plate wall itself such that from 35 to 50 nodes comprised the injector orifice. This orifice was modeled as rectangular for computational ease. Injectant mass flow was matched to the experimental mass flow to within 3provided by the parabolized Navier-Stokes version of the code. Incoming boundary layer thickness was carefully matched to the experimental value to within 5the computational domain were allowed to be free. As noted previously, the solution involved passing an outflow plane from the elliptic solution to the marching code for downstream calculations.

Shown in figure 40 is a plot of computed maximum helium concnetration versus axial distance downstream of the injection point for 30 degree helium injection. Also shown are three experimental data points at each of three axial stations (20, 40, and 90 jet diameters downstream of the jet). The computed helium decay is in excellent agreement with the data. Figure 41 shows computed versus experimentally measured centerline mole fraction of helium at the same three axial locations. The plots represent vertical surveys above the plate surface. Agreement for all three locations is seen to be excellent with the slight discrepancy near the plate $(Z/D = 0)$ due most likely to the parabolized code and inadequacies in the turbulence model. Shown in figure 42 is a plot of computed maximum helium concentration versus axial distance for the case of 15 degree helium injection. Figure 43 displays the centerline mole fraction versus Z/D for three axial locations downstream of the jet. Again, agreement is excellent.

This agreement with experiment shows the ability of the codes to predict in engineering detail both near and far-fields of injection flows - even given the very thorny

problems of grid convergence and turbulence modeling. In addition, detailed examination of the computations indicates that the near-field fuel mixing is controlled largely by large counter-rotating vortices which begin at the jet boundary and strongly deform the jet core. Additional studies are now being performed to further clarify the complicated physics and flow losses which result from single injectors in supersonic air streams.

Generic Scramjet Combustor

Following the two-dimensional mixing enhancement studies and the three-dimensional single wall injector problems discussed in previous sections, a three-dimensional analysis was undertaken to study the generic model scramjet combustor described in figure 44. Each of the four combustor walls contains a step 2.0 cm high located 1.5 cm downstream of the inlet. Four hydrogen fuel injectors are located on each step. One wall has been removed in the figure so that the internal structure can be seen. Air enters the combustor from an upstream inlet at Mach 2.5, a static temperature of 2000 K, and a pressure of 0.101 MPa (1 atm). Gaseous hydrogen fuel is injected under choked conditions at Mach 1.0 at a temperature of 250 K and a pressure of 0.203 MPa. It can be seen from figure 44 that the combustor is symmetric about transverse and spanwise planes through its centerline. Therefore, only one quadrant of the combustor was considered in the analysis. That region is diagrammed in figure 45.

The combustor flow field was solved using the fourth-order compact scheme described earlier in the chapter. The computational grid used in the combustor study had 61 points in the streamwise direction and 45 points in both the transverse and spanwise directions. In the streamwise direction, the points were concentrated at the step and they were exponentially stretched away from the step. In both the transverse and spanwise directions, the points were compressed at the walls and at the steps. An exponentially expanding grid was then connected to the inner grid to span the region from the step to the combustor centerline. The entire grid was also adjusted to account for transverse and spanwise growth

of the fuel jets.

To specify boundary conditions, the wall velocities were set to zero and the wall temperature was set to 1100 K. The boundary layer assumption on pressure was also employed to specify zero pressure gradients on all walls. The walls were also assumed to be non-catalytic such that the gradient of each chemical species vanished at the walls. Symmetry conditions were used at the two symmetry planes. The inflow plane was supersonic, so the velocities, temperature, pressure, and species distributions were specified and held fixed at that location. At the outflow plane, the flow was again supersonic, so extrapolation of velocity, temperature, pressure, and species from upstream values was employed.

The turbulence field in the combustor calculation was modeled using the Baldwin-Lomax turbulence model [34]. Following the work of Riggins [67], the turbulent Schmidt number was assumed to be 0.5. The calculation, carried out initially without chemical reaction, required approximately 3 hours on the NASA Langley Cray 2 computer. The resulting hydrogen mass fraction contours at six successive streamwise stations, beginning near the steps and ending near the combustor outflow boundary, are shown as a contour plot in figure 46. The contour levels range from 0.0 to 1.0 in increments of 0.1. The flow direction is from right to left. The contour levels on the initial plane show high hydrogen concentrations in the vicinity of the four fuel injectors. The hydrogen from each injector mixes with the inlet air with increasing streamwise distance until the near-wall region has nearly uniform levels of hydrogen. It is important to note that the hydrogen from all the injectors remains in the region within one step height from each wall. The shear layer and expansion around the step confines the injected hydrogen to this region, and no penetration into the free stream is achieved. It is also interesting to note that the injectors located near the corner are effectively swept by the strong vortical flow moving into the corner. The hydrogen is mixed very effectively with inlet air in that region, but the vorticity also tends to hold the mixture in the corner. The injectors away from the corner are not affected by the corner vorticity, and they mix much more slowly.

The combustor flow field was next studied with chemical reaction of the hydrogen fuel and air. Only the two injectors near the corner were considered in this study to make the problem more computationally tractable. The two injectors away from the corner were eliminated. Otherwise, the combustor geometry and flow conditions remained unchanged. The 9 species, 18 reaction chemistry model, described in Table 1 was used to model combustion processes. The governing equations were solved on a grid with 41 points in the streamwise direction and 25 points in the transverse and spanwise directions. This grid appeared adequate to resolve important convective effects. Further study on finer grids is planned to more adequately resolve fine-scale mixing and chemical reaction. Solution times were approximately one hour on the Cray 2.

Results from the reacting flow study are shown in figures 47 through 51. The results are represented in the same manner as those shown in figure 46. In this case the flow direction is chosen to be from left to right to more clearly represent the contours. Contours of streamwise velocity are shown in figure 47. The velocity ranges from 1177 m/s to 2504 m/s and the contours are divided into 10 levels. The flow separates in the corner through the fifth cross-stream plane and reattaches beyond that point. Boundary layers form and grow along each wall with typical thickening in the corner region. The temperature field in the combustor is shown in figure 48. Temperature is contoured between 142 K and 2617 K with 10 contour levels. As before, cold hydrogen fuel is pumped into the corner by the corner vortices. Contour structure in the corner representing the cold hydrogen can be seen in the second data plane. Further downstream, the hydrogen begins to mix with hotter air at the third data plane, the fuel-air mixture ignites, and reaction occurs in the corner region from that point downstream. The hydrogen mass fraction distribution is shown in figure 49. The hydrogen mass fraction ranges between 0.1 and 1.0 over 10 contour levels. As noted earlier, hydrogen is forced by the corner vortices into the corner. The fuel then begins mixing with air, and by the seventh data station it is completely consumed to form water. The resulting water mass fraction is shown in figure 50. Water mass fraction

44

is plotted between 0.05 and 0.30 over 10 contour levels. Small amounts of water begin to form a small distance downstream of the injectors well away from the corner on the edge of the fuel jets. Somewhat further downstream, a small amount of water begins to appear in the immediate vicinity of the corner that is convected upstream by the recirculation in the separated flow. By the fifth data plane in the figure, fuel and air have become well mixed and large amounts of water are formed. Reaction is nearly complete at the last data plane shown in the figure.

Fuel-Air Mixing Enhancement

A number of approaches have been suggested for enhancing the mixing of high-speed fuel-air flows. Several of these approaches were discussed in the introduction. A particularly attractive option has been suggested by Northam, Greenberg, and Byington [63]. In their paper, the authors discuss an experimental study of wall-mounted parallel injector ramps used to enhance the relatively slow mixing of fuel and air normally associated with parallel fuel injection. Parallel injection may be useful at high speeds to extract energy from hydrogen that has been used to cool the engine and the airframe of a hypersonic cruise vehicle. The ramp injector configurations were intended to induce vortical flow and local recirculation regions similar to the rearward facing step that has been used for flameholding in reacting supersonic flow.

Two ramp configurations were considered in the experiment. They are both shown in figure 51 which was taken from reference [63]. In both configurations, hydrogen gas was injected at Mach 1.7 from conical nozzles in the base of the two ramps that were inclined at 10.3 degrees to the combustor wall. The injector diameters were 0.762 cm. The sidewalls of the unswept ramps were aligned with Mach 2.0 streamwise air flow from a combustion facility, whereas the swept ramps were swept at an angle of 80 degrees. Each ramp was 7.0 cm long and ended in a nearly square base 1.52 cm on a side. Both ramp designs were chosen to induce vorticity to enhance mixing and base flow recirculation to

provide flameholding. The swept ramp injector, due to its delta shape, was intended to induce higher levels of vorticity and, therefore, higher levels of mixing. Hydrogen injection occurred at a streamwise velocity of 1747 m/s, a transverse velocity of 308 m/s, and a static temperature and pressure of 187 K and 325200 Pa, respectively. The facility air crossed the leading edge of the wedges at a streamwise velocity of 1300 m/s, a static temperature of 1023 K, and a static pressure of 10200 Pa. The air was vitiated following heating by a burner with oxygen, nitrogen, and water mass fractions of 0.2551, 0.5533, and 0.1818, respectively. The overall fuel-air equivalence ratio for the experiment ranged from .3 to 1.5. Other experimental and facility details are given in reference [63].

Both the unswept and swept parallel injector ramps were studied computationally. Only fuel-air mixing was considered in this study. The fourth-order accurate compact algorithm in the program was again used. The facility test section surrounding the ramps and considered in the computation was 13.97 cm long and 3.86 cm high. Symmetry planes were chosen to pass transversely through each fuel injector to define the spanwise computational boundaries. That region was spanned by a computational grid with 43 points in the streamwise direction and 61 points in the transverse and spanwise directions, respectively. The grid was compressed such that each injector was represented by 220 points. No slip boundary conditions were specified on the lower facility wall and on the ramp walls. Free slip boundary conditions were employed on the upper facility wall. Initial calculations were carried out assuming only laminar diffusion.

Results from the computational study for both the unswept and swept injector ramps are shown in figures 52 through 60. Pressure contours through a cross-plane through the center of the injector are given for the unswept and swept ramps in figures 52a and 52b, respectively. The ramp shock, expansion fan at the end of the ramp, and the plume of the fuel jet can be seen in both cases. The swept ramp exhibits a greater shock angle as compared to the unswept ramp because flow more readily spills further upstream about the unswept wedge due to its more narrow spanwise dimension. The predicted shock angle

46

in both cases agrees with the experiment.

Figures 53 through 55 show the cross-stream velocity vectors for the unswept and swept cases at three successive downstream planes (x = 6.60, 8.06, and 13.20 cm) oriented perpendicular to the test section walls. Part (a) of the figures displays the unswept ramp results, and part (b) of the figures displays the swept ramp results. The planar cut extends from the lower to the upper wall of the test section, and it slices through the center of the right fuel jet. The left boundary is located half way between the two ramps. At the x = 6.6 cm station, which lies just ahead of the end of the ramps, a streamwise vortex has formed at the edge of each ramp. The vortex formed by the swept ramp is considerably larger, however, and it persists well into the flow above the ramp and to the ramp centerline. This condition continues at the x = 8.06 cm station located around 1 cm downstream of the end of the ramps. The swept ramp vortex has now begun to interact with the hydrogen fuel jet enhancing its penetration into the air stream. The pluming of the higher pressure fuel jets into the air can also be seen in both cases. At the x = 13.20 cm station, located 6.2 cm beyond the end of the ramps, the swept ramp vortex has continued to grow and has moved further toward the jet centerline. There is pronounced fuel-air mixing enhancement as the vortex spreads across the test section pumping hydrogen fuel into the air stream. Some enhancement is also provided by the unswept ramp, but it is not so nearly pronounced as that provided by the swept ramp.

The transport of hydrogen fuel into the air stream can be seen more clearly by studying the location of hydrogen mass fraction contours in several test section cross-planes that are plotted with increasing streamwise distance. Figures 56 through 60 show the hydrogen mass fraction contours at five successive downstream planes (x = 7.3, 8.06, 9.6, 11.3, and 13.2 cm) again oriented perpendicular to the test section walls. As before, part (a) of the figures displays the unswept ramp results, and part (b) of the figures displays the swept ramp results. The results in figure 56 occur 0.3 cm downstream of the end of the ramp. With the swept ramp, the larger streamwise vortex has already begun to sweep

the hydrogen fuel across into the air stream and away from the lower wall. The smaller streamwise vortex of the unswept ramp also begins to transport hydrogen away from the jet, but not nearly so much as does the swept ramp. As a result, more hydrogen is transported toward the lower wall boundary layer in the unswept case. The same trends continue at the x = 8.06 cm and 9.6 cm stations as shown in figures 57 and 58, respectively. At x = 11.3 cm, as shown in figure 59, the swept ramp enhancer has lifted the fuel jet almost completely off the lower wall. Significant amounts of hydrogen have also been carried across the test section. On the other hand, the unswept ramp enhancer still allows a large amount of hydrogen to be transported along the lower wall, and the spanwise transport is not nearly so great. At x = 13.2 cm, the final streamwise station shown in figure 60, the spanwise spread of the fuel jet enhanced by the swept ramp is 46 percent greater than the spanwise spread due to the unswept ramp. In addition, the swept enhancer has resulted in the fuel jet being transported completely off the lower wall. Finally, an eddy of hydrogen has broken completely away from the primary hydrogen jet, increasing the fuel-air interfacial area even further. Clearly then, the swept ramp enhancer significantly increases the overall spread and mixing of the hydrogen fuel jets. Shown in figure 61 is a plot of mixing efficiency for both swept and unswept ramp injectors (laminar mixing only). This computation included a diverging downstream duct (about 1.25 meters long) which was computed using the parabolized version of the code. Two different regions of the mixing curve are noticable in this figure. The first part of the curve shows rapid near-field mixing due to vortex action and base effects. Downstream, however, the vorticity decays and the diffusive mechanisms predominately control the mixing such that the mixing is considerably smaller. The transistion between these two regions is quite rapid. This mixing behavior, in general, is very similar to that of a normal jet flow-field.

A final mixing study of both the unswept and swept ramp enhancers was undertaken with turbulent flow. As before, turbulence was modeled using the Baldwin-Lomax turbulence model. Results are given in figure 62 at x = 13.2 cm, the final downstream station.

The trends observed in the laminar calculation are also observed here for both cases, with approximately a 43 percent improvement in spanwise spread of the fuel jet enhanced by the swept ramp. The turbulent processes diffuse the interior region of each jet, however, as compared to the laminar result. Because gradients are somewhat relieved by turbulence, the swept ramp no longer bursts the fuel jet as occurred with laminar flow. Therefore, with turbulent flow as described by the present turbulence model, the swept ramp still remains quite attractive as a fuel-air mixing enhancer.

Finally, an analysis of the swept ramp case with finite-rate reaction was completed and results were compared with available experimental data. This work is more completely described by Riggins, McClinton, and Drummond [68]. The reaction mechanism used for the computations was a simple two-step model which allowed relatively efficient CPU time per iteration. The elliptic solution was extended an additional 7.1 centimeters in order to allow for downstream interaction due to high combustion-induced pressures. For this reacting study a full three-dimensional turbulent solution was obtained from the upstream facility nozzle throat to the beginning of the injector ramps. This solution provided an accurate inflow plane for the complex injection region. Again, as in the mixing studies for the single wall jets described in a previous section, the parabolized code was used to solve the downstream flow after a converged elliptic solution was obtained in the injector region. Figure 63 shows computed and experimentally measured wall pressures on the duct centerline for a range of x stations (x = 0 corresponds to the leading edge of the injection ramps). Agreement in both peak pressures and downstream trends is seen to be good for the case shown. Combustion slightly increased near-field mixing over the non-reacting case; this may be due to combustion pressure-induced 'lifting' of the base hydrogen jet more fully into the shed vortex from the swept side of the ramp.

Concluding Remarks

Research has been undertaken in this study to achieve an improved understanding

of important physical phenomena present when a supersonic flow undergoes chemical reaction. To explore the behavior of such flows, detailed physical models of convective and diffusive mixing and finite-rate chemical reaction in supersonic flow were developed. Numerical algorithms were then constructed to solve the equations governing supersonic chemically reacting flow that resulted from these models. Computer programs were written using the algorithms, and each program was used to study a spatially developing and reacting supersonic mixing layer. The results obtained from these studies were then analyzed, and conclusions were drawn concerning the structure of the reacting mixing layer. Those conclusions are now summarized.

Supersonic reacting flows exhibited many of the same features observed for subsonic reacting and nonreacting flows. As in subsonic flows, exothermic heat release in unconfined supersonic flows retarded fuel/air mixing. The vortical structure of the flow, noted in much of the subsonic nonreacting flow literature, was shown to be quite predominant in supersonic reacting flow as well. In agreement with the earlier reacting subsonic literature, the vortical structure had a marked effect on chemical reaction in supersonic flow. Significant burning took place in the eddies on the edges of the mixing layer, broadening the reaction zone relative to the layer thickness defined by the velocity gradient. In addition, the vortical flow resulted in the roll up of unburned reactants inside a layer of partially or fully burned products. This phenomenon, often termed "unmixedness" in subsonic flows, prohibited the reaction of captured reactants and reduced the overall efficiency of the combustion process. Unmixedness was thus shown to be a potential problem in reducing the efficiency of supersonic combustion as well as subsonic combustion, and techniques are needed to overcome it's negative effects on mixing and combustion efficiency.

Because of this need for mixing enhancement in supersonic reacting flows, techniques for enhancing fuel-air mixing and combustion were also explored in this chapter. The initial studies were limited to two dimensions. A supersonic spatially developing and chemically reacting mixing layer well represents the early stages of mixing and reaction that take

50

place in a scramjet combustor. The mixing layer was therefore considered as a model problem for the initial phases of this study. Once this problem was chosen, a simulation of a reacting mixing layer without enhancement was first performed using the computer code to serve as a benchmark for the enhancement studies that followed. Two calculations employing enhancement were then carried out, the first employing planar shocks and the second employing a shock with curvature. The second enhancement approach proved more attractive. The curved shock produced vorticity when it interacted with the high velocity gradient in mixing layer and a higher degree of mixing and reaction then resulted. Based on the results of this study, an alternate fuel injector configuration employing interacting jets was computationally designed. That configuration significantly increased the amount of fuel-air mixing and reaction over a given combustor length that was achieved.

The study was then extended to three dimensions and simple wall injection cases were modeled both to validate the code as well as to gain an understanding of the injection flow-field. Agreement with available data for such flows is excellent. A technique for enhancing fuel-air mixing and reaction in a scramjet combustor was then explored. The computer program was first used to study fuel-air mixing in a generic scramjet combustor. The design of that combustor did not promote a sufficient degree of fuel penetration and fuel-air mixing. Two parallel injector ramp enhancement configurations, one swept and the other without sweep, were then considered to assess their ability to provide a sufficient degree of fuel-air mixing and mixing efficiency. The swept injector ramp configuration induced a large degree of streamwise vorticity, and significantly increased the amount of fuel-air mixing that was achieved as compared to the unswept configuration. The swept injector ramp therefore appeared to be an attractive option for mixing and combustion enhancement in a scramjet combustor.

References

[1] Drummond, J. Philip; Rogers, R. Clayton; and Evans, John S.: Combustor Modelling for Scramjet Engines. *Combustor Modelling,* AGARD-CP-275, Feb. 1980, pp. 10-1–10-30.

[2] Drummond, J. Philip; and Weidner, Elizabeth H.: Numerical Study of a Scramjet Engine Flowfield. *AIAA J.,* vol. 20, no. 9, Sept. 1982, pp. 1182–1187.

[3] Drummond, J. Philip: Numerical Study of a Ramjet Drump Combustor Flowfield. *AIAA J.,* vol. 23, no. 4, Apr. 1985, pp. 604–611.

[4] Carpenter, Peter W.: A Numerical Investigation Into the Effects of Compressibility and Total Enthalpy Difference on the Development of a Laminar Free Shear Layer. *J. Fluid Mech.,* vol. 50, pt. 4, Dec. 29, 1971, pp. 785–799.

[5] Brown, Garry L.; and Roshko, Anotol: On Density Effects and Large Structure in Turbulent Mixing Layers. *J. Fluid Mech.,* vol. 64, pt. 4, July 24, 1974, pp. 775–816.

[6] Roshko, A.: Progress and Problems in Understanding Turbulent Shear Flows. *Turbulent Mixing in Nonreactive and Reactive Flows,* S. N. B. Murthy, ed., Plenum Press, c.1975, pp. 295–316.

[7] Freziger, Joel H.; and McMillian, O. J.: *Studies of Structure and Modeling in Turbulent Shear Flows.* NEAR TR 335 (Contract No. N00014-82-C-0672), Nielsen Engineering and Research, Inc., Dec. 1984. (Available from DTIC as AD A151 807.)

[8] Oh, Y. H.: Analysis of Two-Dimensional Free Turbulent Mixing. AIAA Paper No. 74-594, June 1974.

[9] Papamoschou, D.; and Roshko, A.: Observations of Supersonic Free Shear Layers. AIAA-86-0162, Jan. 1986.

[10] Hussaini, M. Y.; Collier, F.; and Bushnell, D. M.: Turbulence Alteration Due to Shock Motion. *Turbulent Shear-Layer/Shock-Wave Interactions*, J. Délery, ed., Springer-Verlag, c.1986, pp. 371–381.

[11] Yule, A. J.; Chigier, N. A.; and Thompson, D.: Coherent Structures in Combustion. *Symposium on Turbulent Shear Flows*, Pennsylvania State Univ., 1977, pp. 7.41–7.50.

[12] Masutani, S. M.; and Bowman, C. T.: *The Structure of a Chemically Reacting Plane Mixing Layer*. Stanford Univ. paper presented at the Western States Section/Combustion Inst. 1984 Spring Meeting (Boulder, Colorado), Apr. 2–3, 1984.

[13] Keller, Jay O.; and Daily, John W.: The Effects of Large Heat Release on a Two Dimensional Mixing Layer. AIAA-83-0472, Jan. 1983.

[14] Mungal, M. G.; Dimotakis, P. E.; and Hermanson, J. C.: Reynolds Number Effects on Mixing and Combustion in a Reacting Shear Layer. AIAA-84-0371, Jan. 1984.

[15] Hermanson, J. C.; Mungal, M. G.; and Dimotakis, P. E.: Heat Release Effects on Shear Layer Growth and Entrainment. AIAA-85-0142, Jan. 1985.

[16] Pitz, Robert W.; and Daily John W.: Combustion in a Turbulent Mixing Layer Formed at a Rearward-Facing Step. *AIAA J.*, vol. 21, no. 11, Nov. 1983, pp. 1565–1570.

[17] Broadwell, James E.; and Dimotakis, Paul E.: Implications of Recent Experimental Results for Modeling Reactions in Turbulent Flows. AIAA-84-0545, Jan. 1984.

[18] Carrier, G. F.; Fendall, F. E.; and Marble, F. E.: The Effect of Strain Rate on Diffusion Flames. *SIAM J. Appl. Math.*, vol. 28, no. 2, Mar. 1975, pp. 463–500.

[19] Riley, James J.; and Metcalfe, Ralph W.: Direct Simulations of Chemically Reacting Turbulent Mixing Layers. AIAA-85-0321, Jan. 1985.

[20] McMurtry, P. A.; Jou, W.-H.; Riley, J. J.; and Metcalfe, R. W.: Direct Numerical Simulations of a Reacting Mixing Layer With Chemical Heat Release. AIAA-85-0143, Jan. 1985.

[21] Menon, S.; Anderson, J. D., Jr.; and Pai, S. I.: Stability of a Laminar Premixed Supersonic Free Shear Layer With Chemical Reactions. *Int. J. Eng. Sci.*, vol. 22, no. 4, 1984, pp. 361–374.

[22] Drummond, J. P.:A Two-Dimensional Numerical Simulation of a Supersonic, hemically Reacting Mixing Layer. NASA TM 4055, 1988.

[23] Carpenter, M. H.: Three-Dimensional Computations of Cross-Flow Injection and Combustion in a Supersonic Flow. AIAA-89-1870, June 1989.

[24] Williams, F. A.; *Combustion Theory.* Addison-Wesley Publishing Company, Inc., Reading, MA, pp. 358-429, 1965.

[25] McBride, B. J.; Heimel,S.; Ehlers, J. G.; and Gordon, S.; Thermodynamic Properties to 6000 K for 210 Substances Involving the First 18 Elements. NASA SP-3001, 1963.

[26] Kanury, A. M.; *Introduction to Combustion Phenomena.* Gordon and Breach Science Publishers, New York, pp. 363-371, 1982.

[27] White, F. M.; *Viscous Fluid Flow.* McGraw-Hill Inc., New York, pp. 28-36, 1974.

[28] Suehla, R. A.; Estimated Viscosities and Thermal Conductivities of Gases at High Temperature. NASA TR R-132, 1962.

[29] Wilke, C. R.; A Viscosity Equation for Gas Mixtures. Journal of Chemistry and Physics, v. 18, no. 4, pp. 517-519, 1950.

[30] Berman, H. A.; Anderson, J. D.; and Drummond, J. P.; Supersonic Flow Over a Rearward Facing Step with Transverse Nonreacting Hydrogen Injection. AIAA Journal, v. 21, no. 12, pp. 1701-1713, 1983.

[31] Kee, R. J.; Warnatz, J.; and Miller, J. A.; A Fortran Computer Code Package for the Evaluation of Gas-Phase Viscosities, Conductivities, and Diffusion Coefficients. Sandia Report SAND83-8209, Mar. 1983.

[32] Schetz, J. A.; Billig, F. S.; and Favin, S.; Flowfield Analysis of a Scramjet Combustor with a Coaxial Fuel Jet. AIAA Journal, v. 20, no. 9, pp. 1268-1274, 1982.

[33] Cebeci, T.; and Smith, A. M. O.; *Analysis of Turbulent Boundary Layers*. Academic Press, New York, 1974.

[34] Baldwin, B. S.; and Lomax, H.; Thin Layer Approximations and Algebraic Model for Separated Turbulent Flows. AIAA Paper No. 78-257, Jan. 1978.

[35] Jones, W. P.; and Launder, B. E.; The Prediction of Laminarization with a Two-Equation Model of Turbulence. International Journal of Heat and Mass Transfer, v. 15, p. 301, 1972.

[36] Fabris, G. ; Harsha, P. T.; and Edelman, R. B.; Multiple-Scale Turbulence Modeling of Boundary Layer Flows for Scramjet Applications. NASA CR-3433, 1981.

[37] Hanjalic, K.; and Launder, B. E.; Sensitizing the Dissipation Equation to Irrotational Strains. Journal of Fluids Engineering, Transactions of ASME, v. 102, pp. 34-40, 1980.

[38] Hanjalic, K.; Launder, B. E.; and Schiestel, R.; Multiple-Time Scale Concepts in Turbulent Transport Modeling. Second Sympsoium on Turbulent Shear Flows, Imperial College, London, July 1979.

[39] Rodi, W.; The Prediction of Free Turbulent Boundary Layers by Use of a Two-Equation Model of Turbulence. Ph.D. Thesis, University of London, 1972.

[40] Sindir, M. M.; Numerical Study of Turbulent Flows in Backward-Facing Step Geometries; Comparison of Four Models of Turbulence. Ph.D. Thesis, University of California, Davis, June 1982.

[41] Oran, E.; and Boris, J.: *Recent Advances in Numerical Methods for Chemically Reacting Flows*. American Institute of Astronautics and Aeronautics, 1990.

[42] Riley, J. J.; Metcalfe, R. W.; and Orszag, S. A.; Direct Numerical Simulations of Chemically Reacting Turbulent Mixing Layers. Physics of Fluids, v. 29, no. 2, pp. 406-422, 1986.

[43] McMurtry, P. A.; Jou, W.-H.; Riley, J. J.; and Metcalfe, R. W.; Direct Numerical Simulations of a Reacting Mixing Layer with Chemical Heat Release. AIAA Journal, v. 24, no. 6, pp. 962-970, 1986.

[44] Erlebacher, G.; and Hussaini, M.Y.; Stability and Transition in Supersonic Boundary Layers. AIAA Paper No. 87-1416, June 1987.

[45] Schumann, U.; Subgrid Scale Model for Finite Difference Simulations of Turbulent Flows in Plane Channels and Annuli. Journal of Computational Physics, v. 18, pp. 376-404, 1975.

[46] Speziale, C. C.; Erlebacher, G.; Zang, T. A.; and Hussaini, M. Y.; On the Subgrid-Scale Modeling of Compressible Turbulence. NASA CR-178420 (ICASE Report No. 87-73), 1987.

[47] Bussing, T. R. A.; and Murman, E. M.; A Finite Volume Method for Calculation of Compressed Chemically Reacting Flows. AIAA Paper No. 85-0311, Jan. 1985.

[48] Widhopf, G. F.; and Victoria, K. J.; On the Solution of the Unsteady Navier-Stokes Equations Including Multicomponent Finite Rate Chemistry. Computers and Fluids, v. 1, pp. 159-184, 1973.

[49] MacCormack, R. W.; The Effect of Viscosity on Hypervelocity Impact Cratering. AIAA Paper No. 69-354, Apr. 1969.

[50] Householder, A. S.: The Theory of Matrices in Numerical Analysis. Dover Publications, New York, 1964, pp. 122-140.

[51] Gottlieb, D.; and Turkel, E.: Dissipative Two-Four Methods for Time-Dependent Problems. Mathematics of Computation, v.30, no. 136, 1976, pp. 703-723.

[52] Abarbanel, S.; and Kumar, A.: Compact High-Order Schemes for the Euler Equations. J. Scientific Computing, v. 3, no. 3, Sep. 1988.

[53] Carpenter, M. H.: A Comparative Study of High-Order and Compact Numerical Algorithms with Existing Central and Upwind Algorithms. NASA CR- , 1990.

[54] Drummond, J. P.; Carpenter, M. H.; Riggins, D. W.; and Adams, M. S.: Mixing Enhancement in a Supersonic Combustor. AIAA-89-2794, July 1989.

[55] Ragab, S. A.; and Wu, J. L.: Instabilities in the Free Shear Layer Formed by Two Supersonic Streams. AIAA Paper 88-0038, Jan. 1988.

[56] Guirguis, R. H.; Grinstein, F. F.; Young, T. R.; Oran, E. S.; Kailasanath, K.; and Boris, J. P.: Mixing Enhancement in Supersonic Shear Layers. AIAA Paper 87-0373, Jan. 1987.

[57] Guirguis, R. H.: Mixing Enhancement in Supersonic Shear Layers: III. Effect of Convective Mach Number. AIAA Paper 88-0701, Jan. 1988

[58] Kumar, A.; Bushnell, D. M.; and Hussaini, M. Y.: A Mixing Augmentation Technique for Hypervelocity Scramjets. AIAA Paper 87-1182, Jun. 1988.

[59] Drummond, J. P.; and Mukunda, H. S.: A Numerical Study of Mixing Enhancement in Supersonic Reacting Flow Fields. AIAA Paper 88-3260, Jul. 1988.

[60] Menon, S.: Shock-Wave-Induced Mixing Enhancement in Scramjet Combustors. AIAA Paper 89-0104, Jan. 1989.

[61] King, P. S.; Thomas, R. H.; and Schetz, J. A.: Combined Tangential-Normal Injection Into a Supersonic Flow. AIAA Paper 89-0622, Jan. 1989.

[62] Sullins, G. A.; Lutz, S. A.; Carpenter, D. A.; and Taylor, M. A.: Experimental Investigation of a Shear Layer in Supersonic Flow. 1989 JANNAF Propulsion Meeting, Cleveland, OH, May 1989.

[63] Northam, G. B.; Greenberg, I.; and Byington, C. S.: Evaluation of Parallel Injector Configurations for Supersonic Combustion. AIAA Paper 89-2525, Jul. 1989.

[64] Schlichting, H.: *Boundary-Layer Theory*. McGraw-Hill, New York, 1968.

[65] Mays, R. B.; Thomas, R. H.; and Schetz, J. A.: Low Angle Injection into a Supersonic Flow. AIAA Paper 89-2461, Jul. 1989.

[66] Kamath, H.: Parabolized Navier-Stokes Algorithm for Chemically Reacting Flows. AIAA Paper 89-0386, Jan. 1989.

[67] Riggins, D. W.; McClinton, C. R.; and Drummond, J. P.: A Numerical Study of Mixing Enhancement in a Supersonic Combustor. AIAA Paper 90-0203, Jan. 1990.

Appendix

Nomenclature

A_j	:	reaction rate constant for jth reaction
b_i	:	body force of species i
C_i	:	concentration of species i
$\dot{C}_i$	:	time rate of change of C_i
c_p	:	specific heat at constant pressure
D_{ij}	:	binary diffusion coefficient
D_T	:	thermal diffusion coefficient
E	:	total internal energy; activation energy
$\vec{E}, \vec{F}, \vec{G}$	:	flux vectors in x, y, and z coordinate directions
f_i	:	mass fraction of species i
g_j	:	Gibbs energy of species i
G_R	:	Gibbs energy of reaction
h	:	height of channel or duct
h_i	:	enthalpy of species i
h_i^o	:	reference enthalpy of species i
$\vec{H}$	:	source vector
K_b	:	backward rate constant
K_f	:	forward rate constant
K_{eq}	:	equilibrium constant
M	:	Mach number
M_i	:	molecular weight of species i
n_i	:	moles of species i
ns	:	number of chemical species
nr	:	number of chemical reactions
p	:	pressure

$\dot{q}$	:	heat flux
R^o	:	universal gas constant
T	:	temperature
T_R	:	reference temperature $= 298^o k$
T_ϵ	:	effective temperature
t	:	time
Δt	:	time step
$\vec{U}$	:	dependent variable vector
u	:	streamwise velocity
v	:	transverse velocity
$\tilde{u}_i$	:	streamwise diffusion velocity of species i
$\tilde{v}_i$	:	transverse diffusion velocity of species i
$\tilde{V}_i$	:	diffusion velocity vector of species i
$\dot{w}_i$	:	species production rate of species i
x	:	streamwise coordinate
y	:	transverse coordinate
X_i	:	mole fraction of species i
λ	:	second viscosity coefficient
γ_{ij}	:	stoichiometric coefficient; species i, reaction j
γ	:	ratio of specific heats
δ	:	Kronecker delta function
ρ	:	density
σ	:	normal stress
σ_{ij}	:	effective collision diameter
τ	:	shear stress
μ_i	:	laminar viscosity of species i
μ	:	mixture laminar viscosity

ξ	:	computational streamwise coordinate
η	:	computational transverse coordinate
Ω_D	:	diffusion collision integral
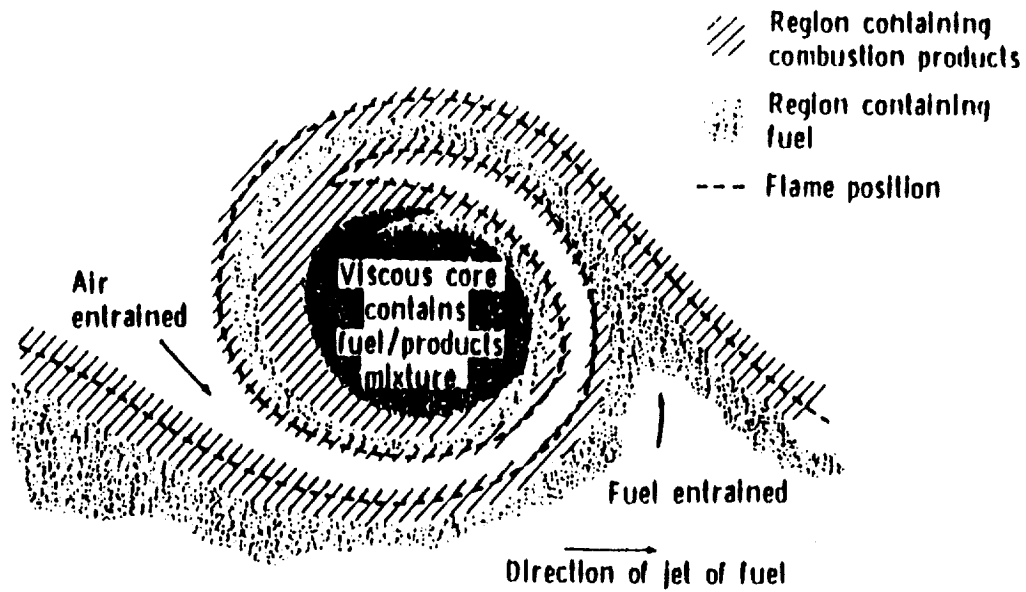
Figure 1. Cross section of transitional vortex eddy
in gas diffusion flame (ref. 11).
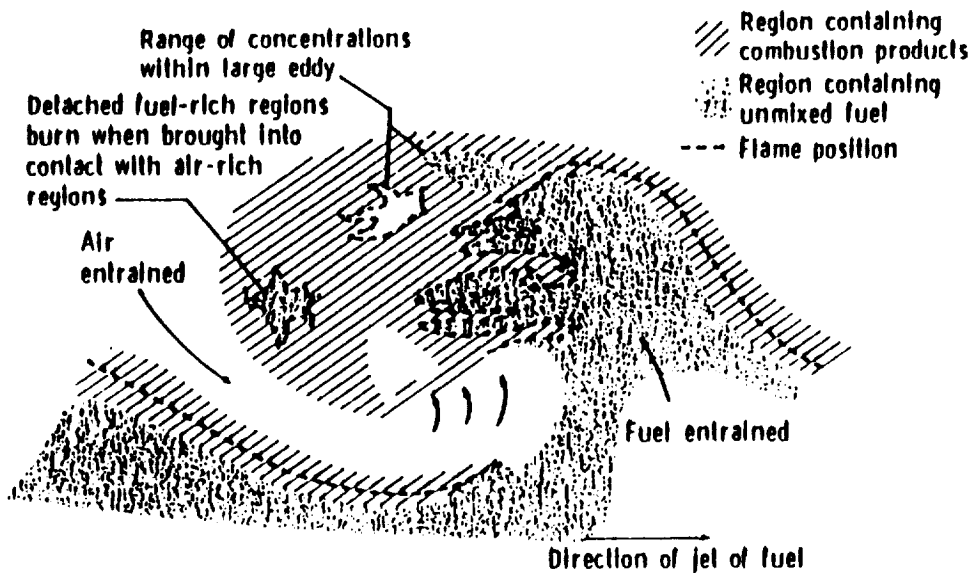
Figure 2. Cross section of large turbulent eddy in
gas diffusion flame (ref. 11).

62
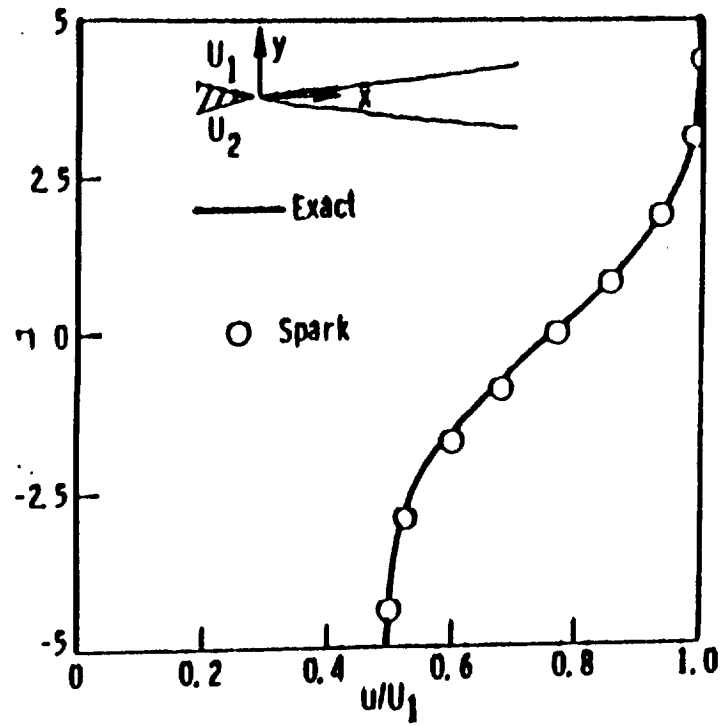
Figure 3. Comparison of exact and numerical solution
of a supersonic shear layer.
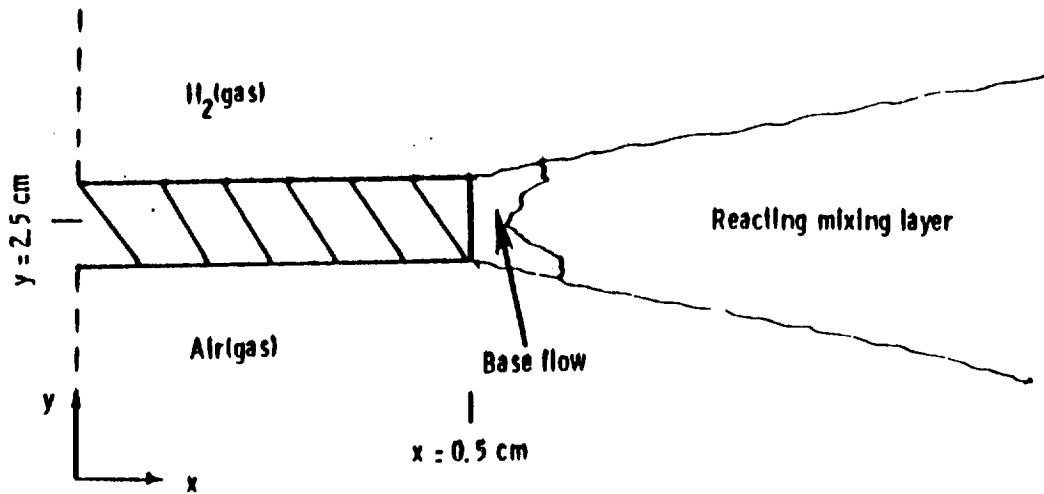
Figure 4. Reacting mixing layer schematic.
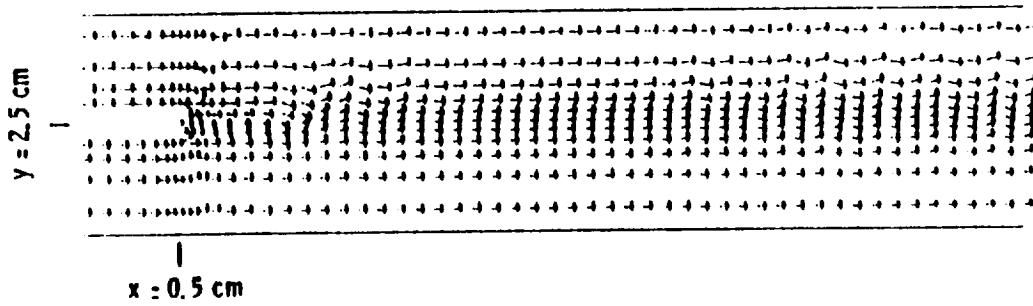
Figure 5. Mixing layer velocity field (every fourth vector plotted (0.1 ms)).
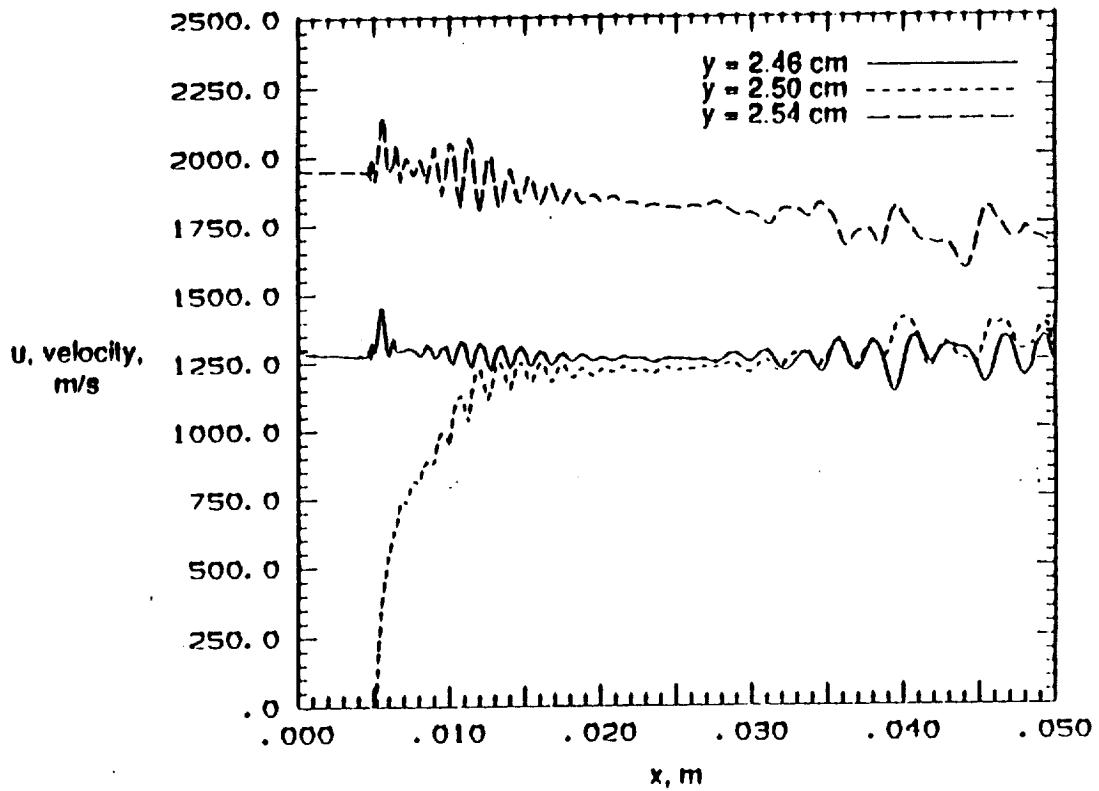
Figure 6. Streamwise velocity versus x at y locations
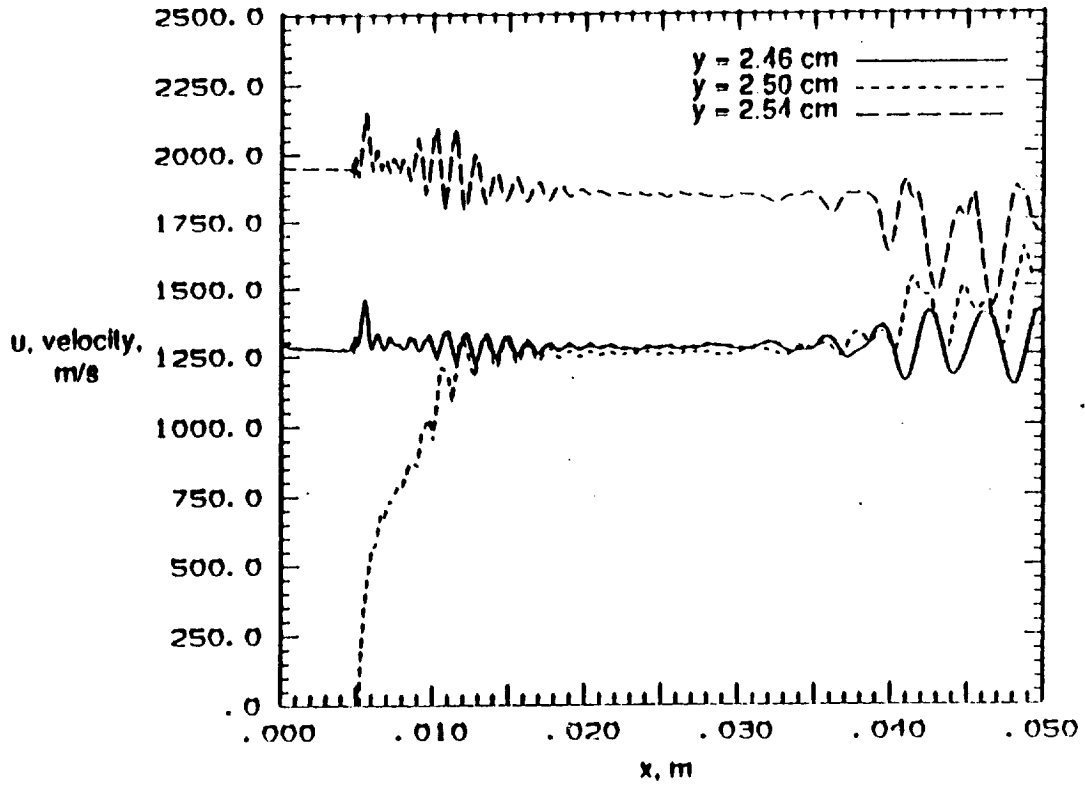
Figure 7. Streamwise velocity versus x at y locations: nonreacting flow (0.1 ms).
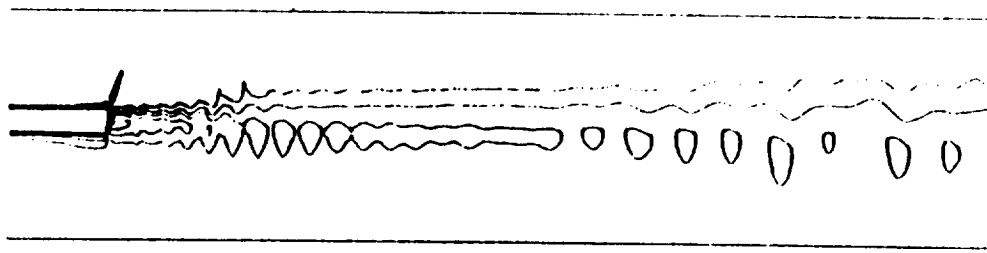
Figure 8. Streamwise velocity contours in mixing layer.

Figure 9. Temperature contours in mixing layer.
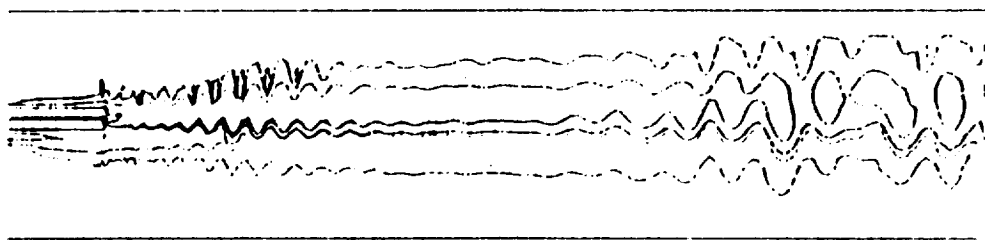
Figure 10. Vorticity contours in mixing layer.
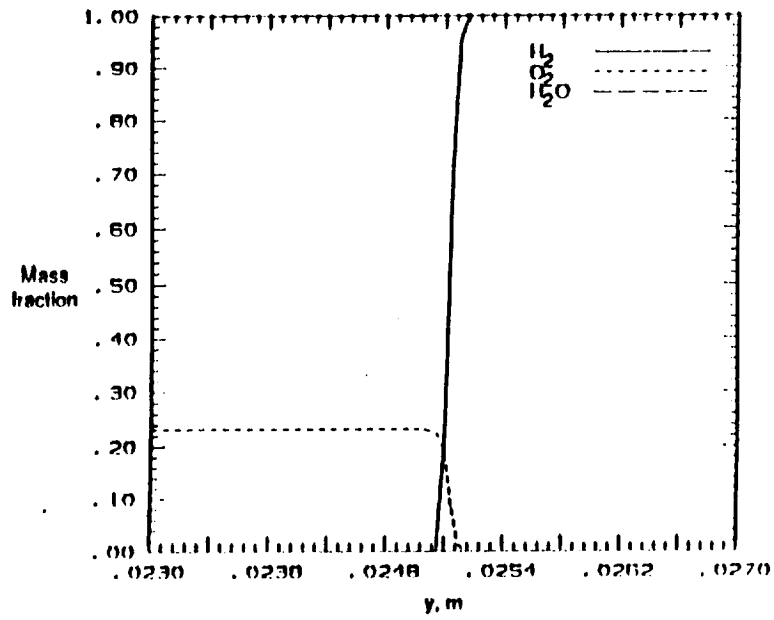
(a) Major species.
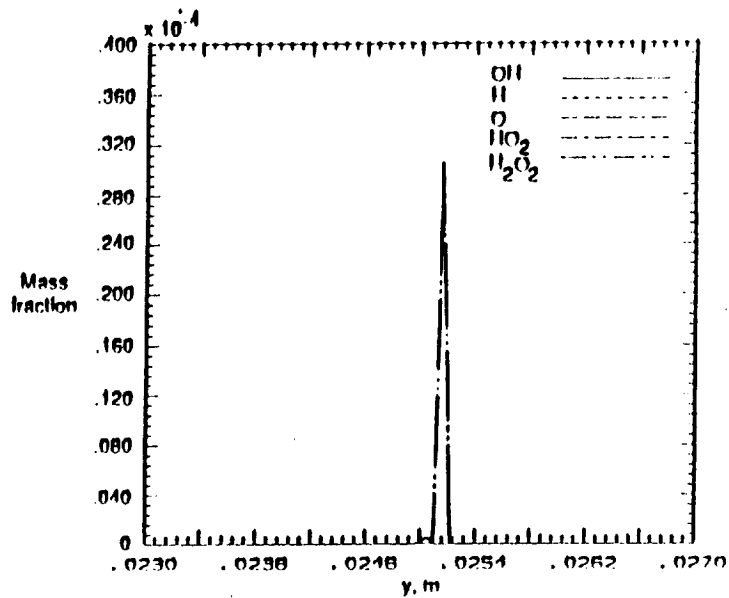
(h) Minor species.

Figure 11. Mass fraction versus y at x=0.51cm.
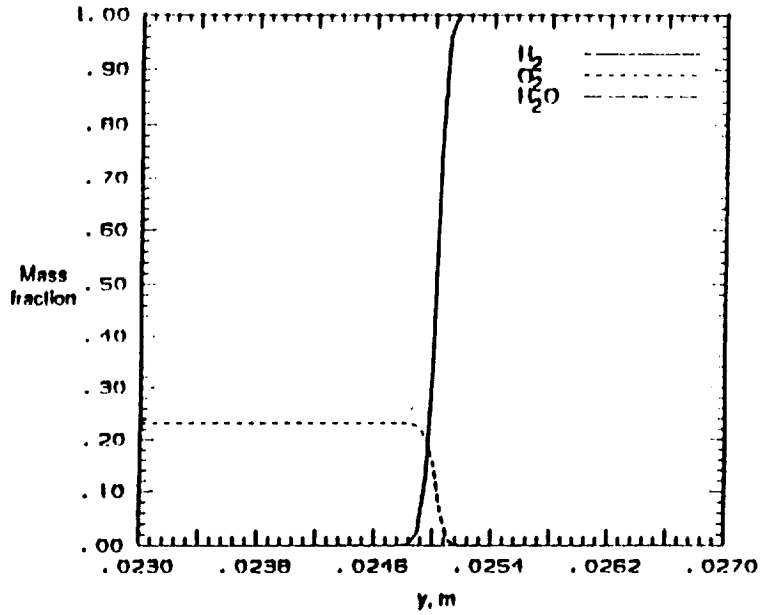
(a) Major species.
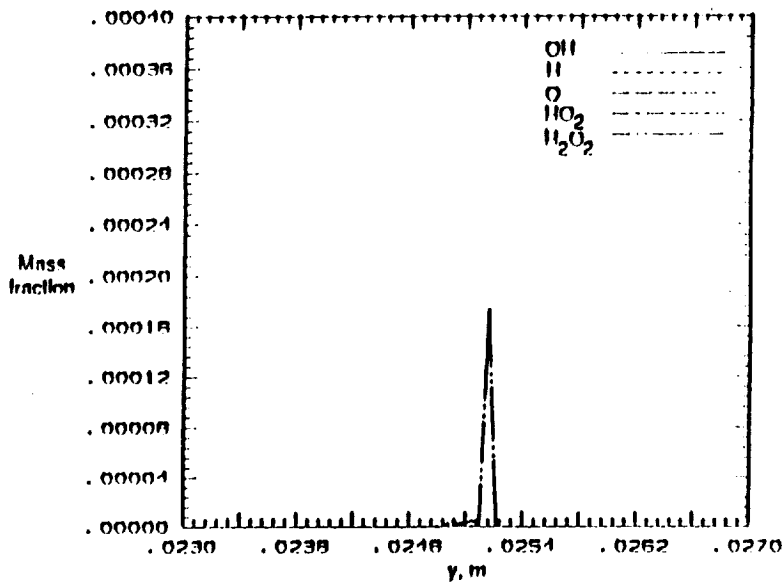
(b) Minor species.

Figure 12. Mass fraction versus y at x=0.58 cm.

68
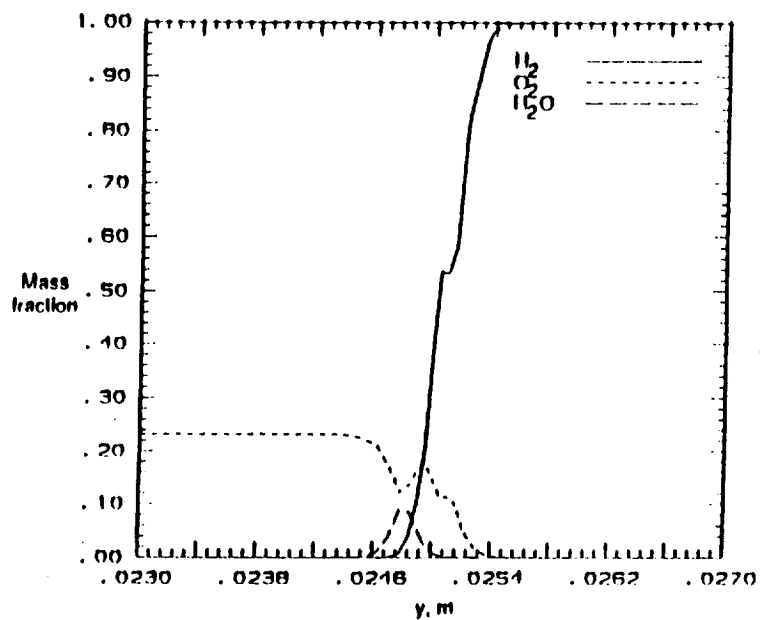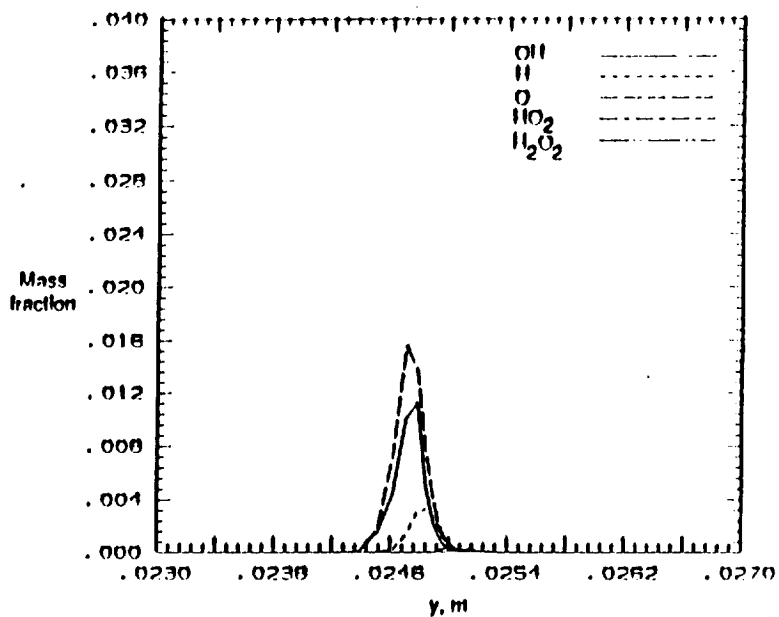
(a) Major species.

(b) Minor species.

Figure 13. Mass fraction versus y at x=1.0 cm.

69
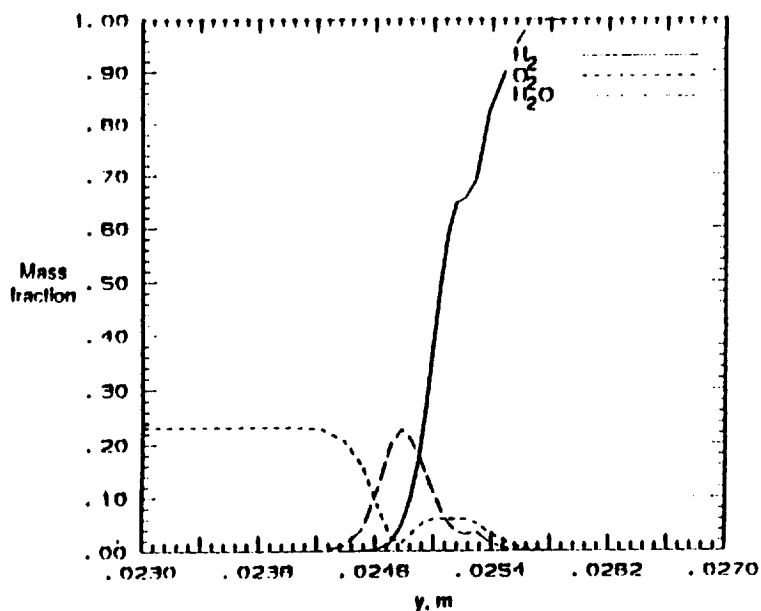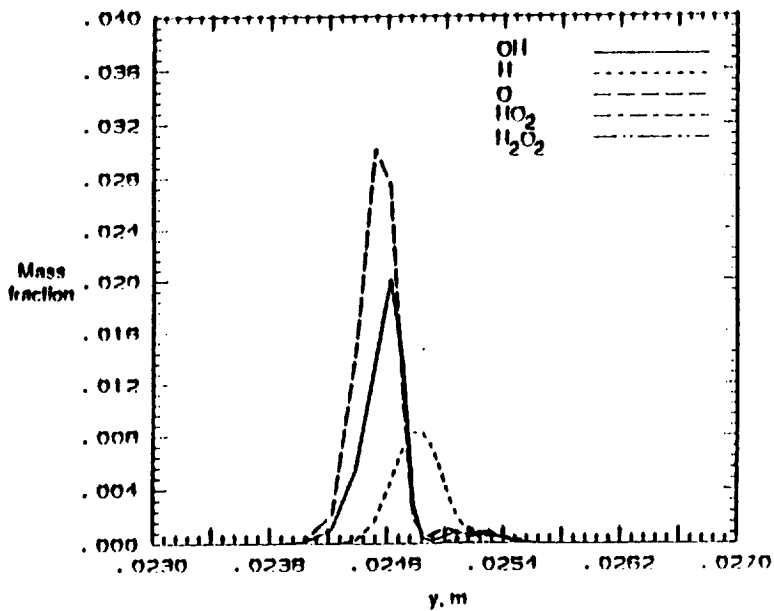
(a) Major species.

(b) Minor species.

Figure 14. Mass fraction versus y at x=2.0 cm.

70
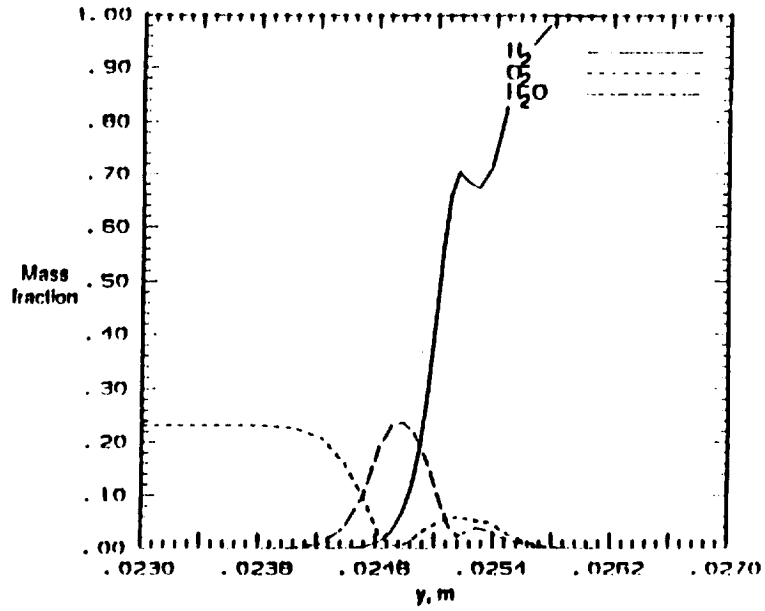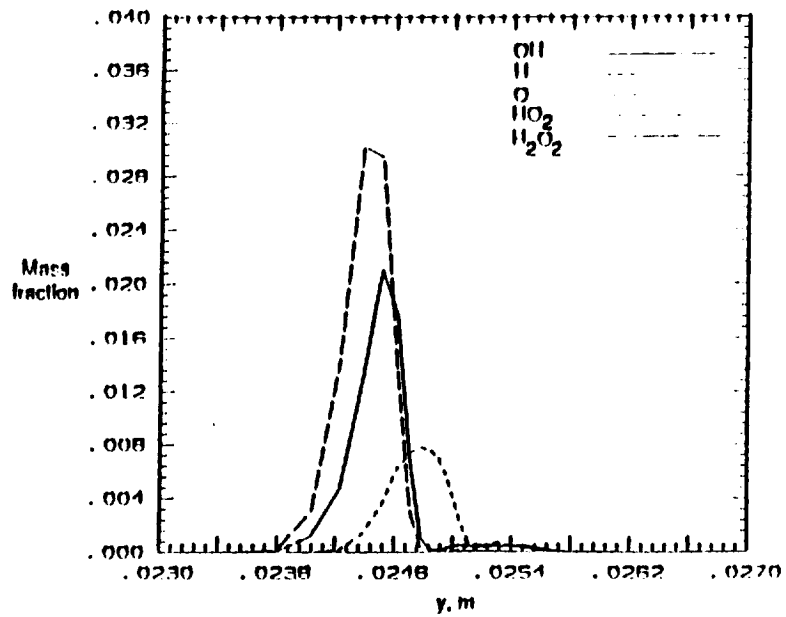
(a) Major species.

(b) Minor species.

Figure 15. Mass fraction versus y at x-3.0 cm.

71
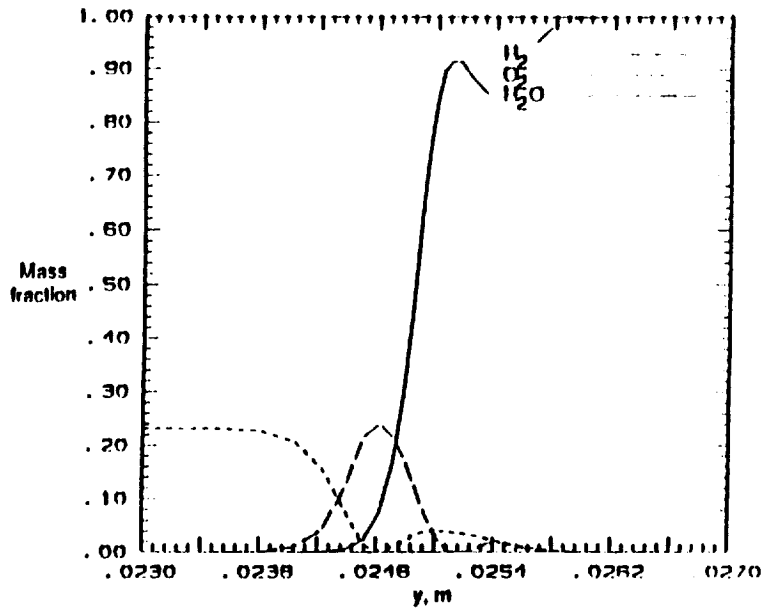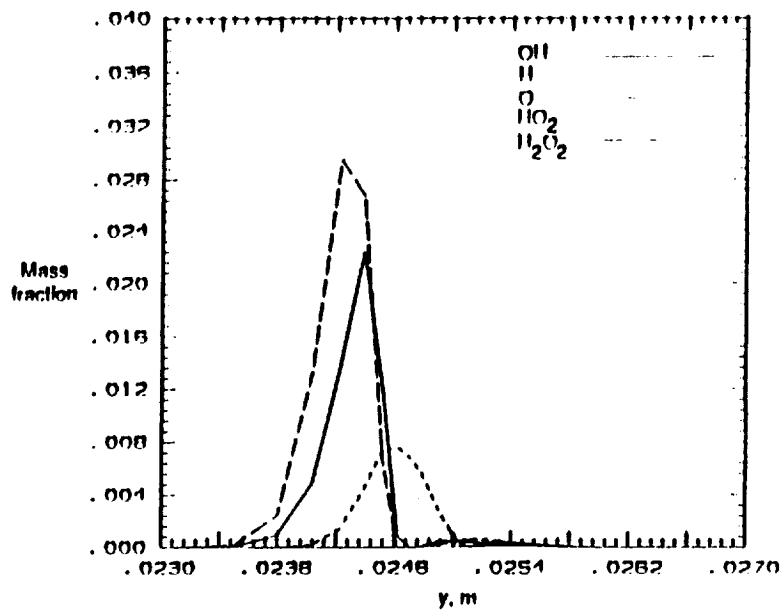
(a) Major species.

(b) Minor species.

Figure 16. Mass fraction versus y at x=4.0 cm.

72
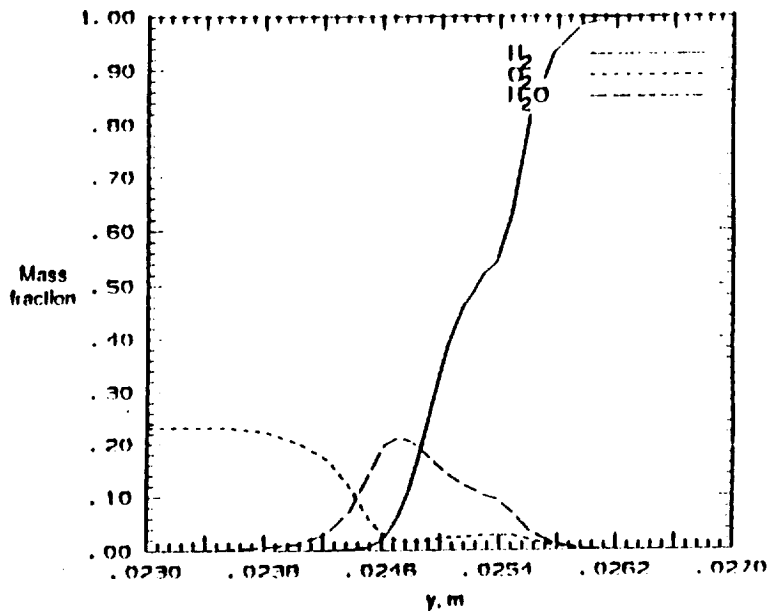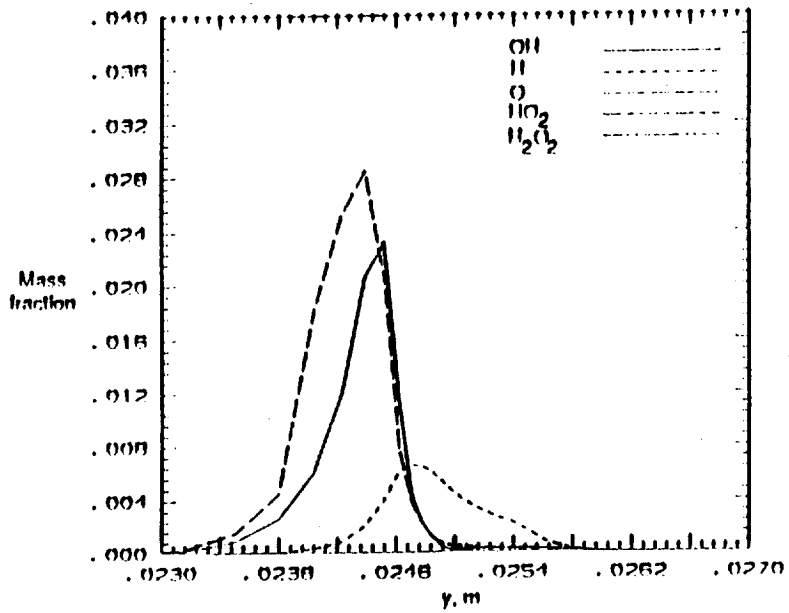
(a) Major species.

(b) Minor species.

Figure 17. Mass fraction versus y at x- 5.0 cm.
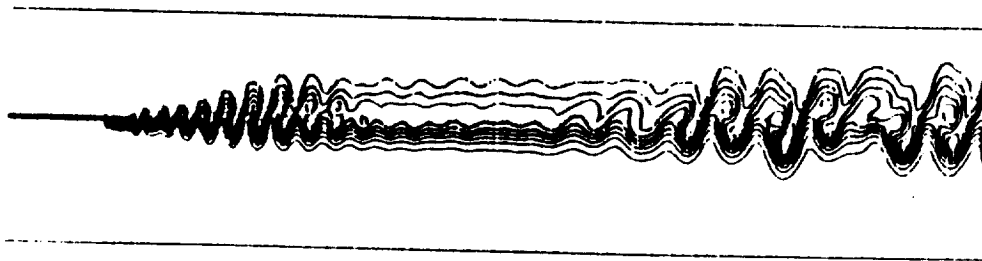
Figure 18. Hydrogen mass fraction contours in mixing layer.
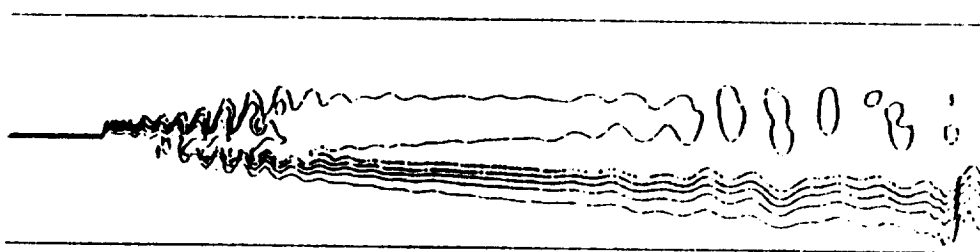
Figure 19. Oxygen mass fraction contours in mixing layer.
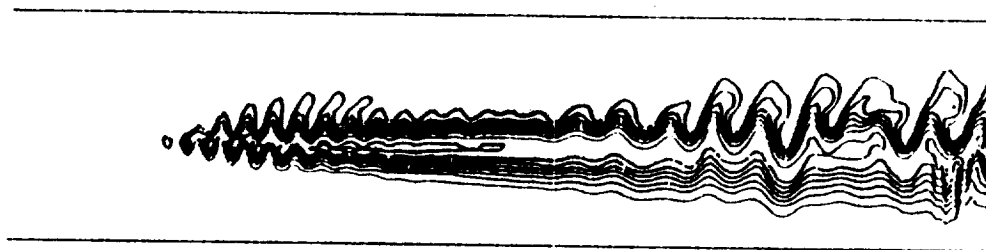
Figure 20. Atomic hydrogen (H) mass fraction contours
in mixing layer.

74
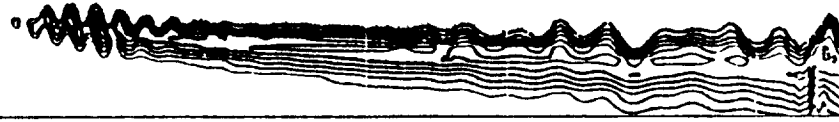
Figure 21. Atomic oxygen (O) mass fraction contours in
mixing layer.

Figure 22. Hydroxyl (OH) mass fraction contours in mixing
layer.
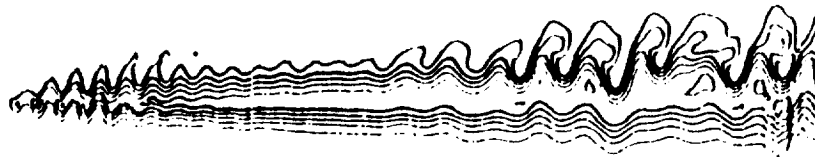
Figure 23. Water mass fraction contours in mixing layer.
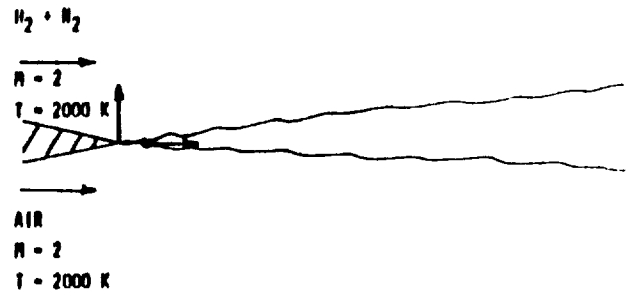
Figure 24. Schematic of the supersonic reacting mixing layer in Case 1.
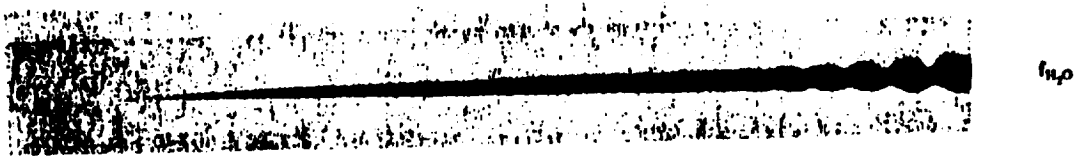
Figure 25. Water mass fraction contours in Case 1.
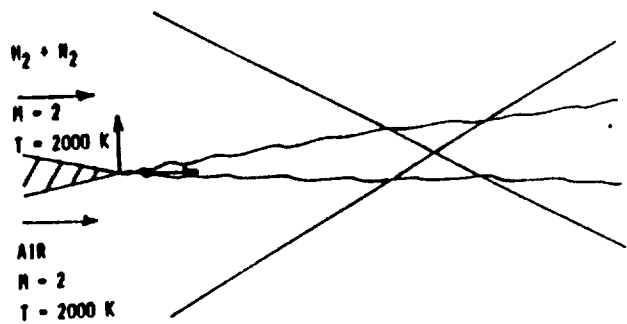
Figure 26. Schematic of the supersonic reacting mixing layer interacting with two shocks in Case 2.

76
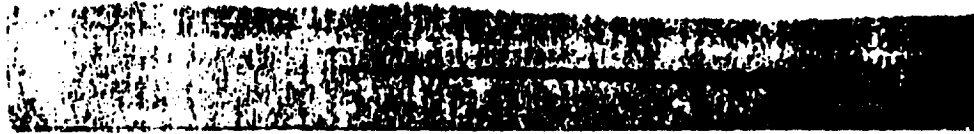
f_{H_2O}

Figure 27. Water mass fraction contours in Case 2.

H$_2$ + N$_2$

M = 2

T = 2000 K

AIR

M = 2

T = 2000 K
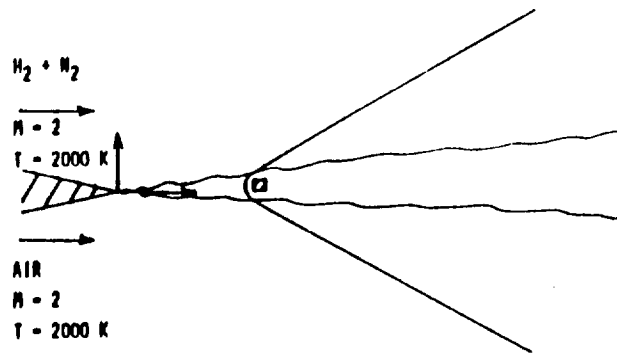
Figure 28. Schematic of the supersonic reacting mixing
layer interacting with a curved shock in Case 3.
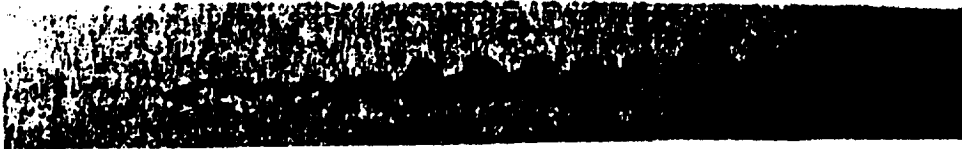
f_{H_2O}

Figure 29. Water mass fraction contours in Case 3.

77
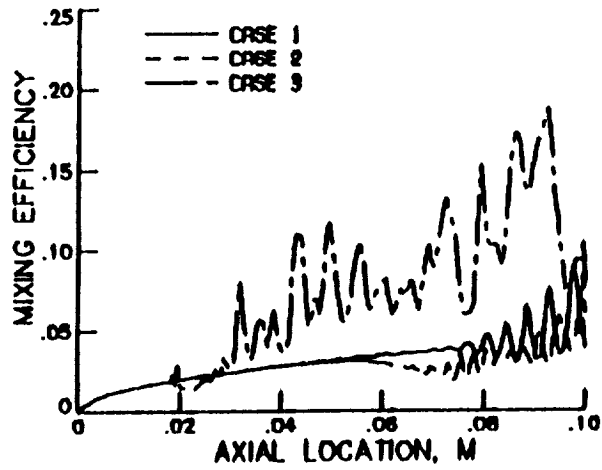
Figure 30. Mixing efficiency versus streamwise station for
Cases 1 through 3.
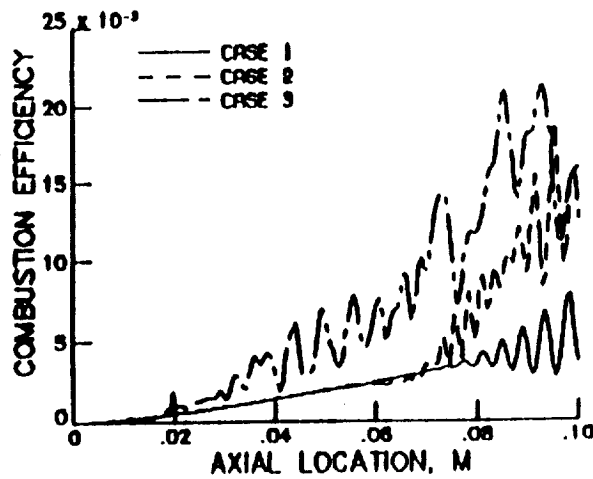
Figure 31. Combustion efficiency versus streamwise station
for Cases 1, 2 and 3.
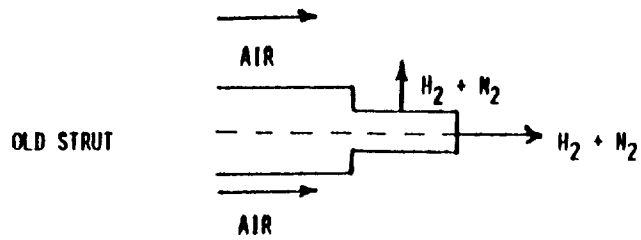
Figure 32. Schematic of conventional fuel injector strut configuration.
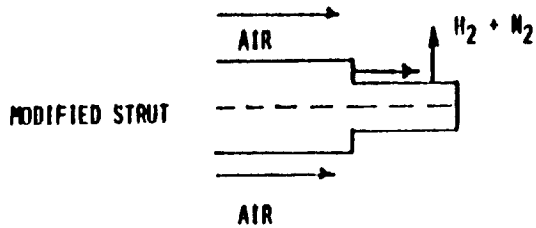
Figure 33. Schematic of modified fuel injector strut configuration.
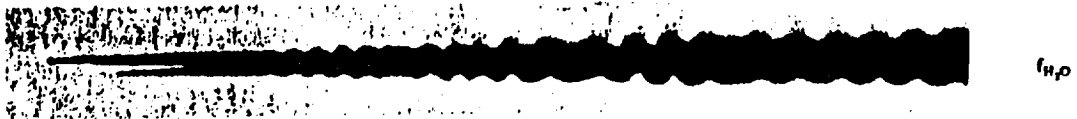
Figure 34. Water mass fraction contours in Case 4 with only the parallel injector.
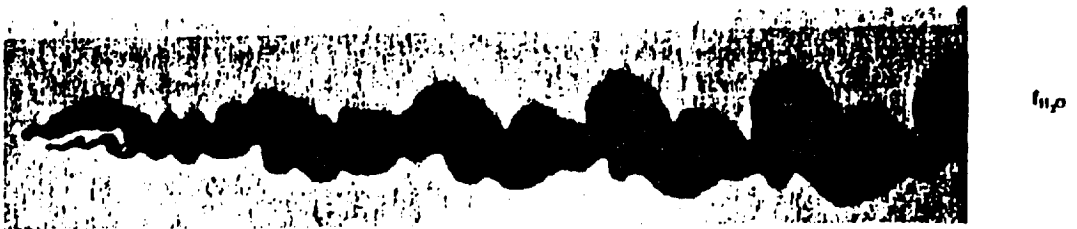
Figure 35. Water mass fraction contours in Case 5 with interaction of the parallel and transverse injectors.
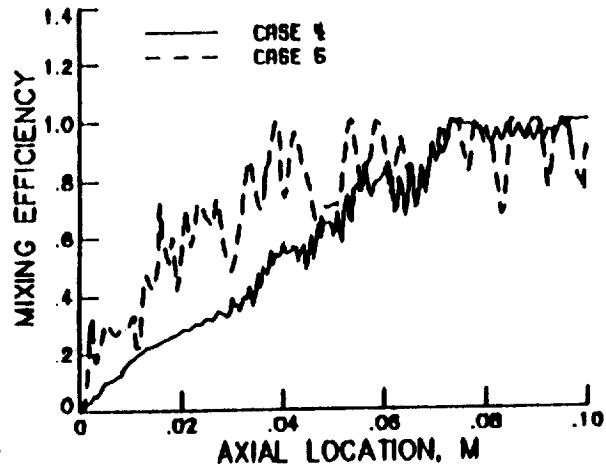
Figure 36. Mixing efficiency versus streamwise station for Cases 4 and 5.
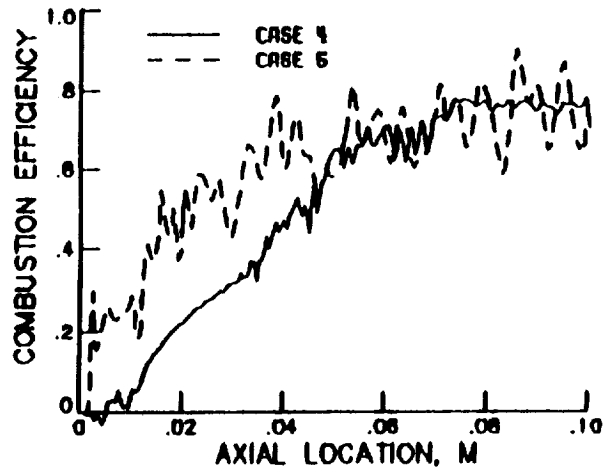
Figure 37. Combustion efficiency versus streamwise station for Cases 4 and 5.

UPSTREAM — | — NEARFIELD — | — FARFIELD

INJECTOR REGION   DOWNSTREAM

M →

PNS   ELLIPTIC   PNS
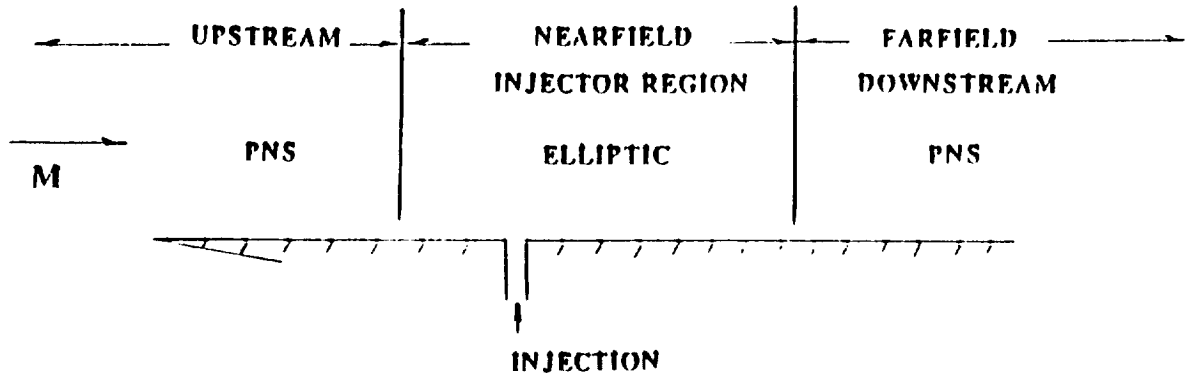
INJECTION

Figure 38. Schematic of flat plate single injection
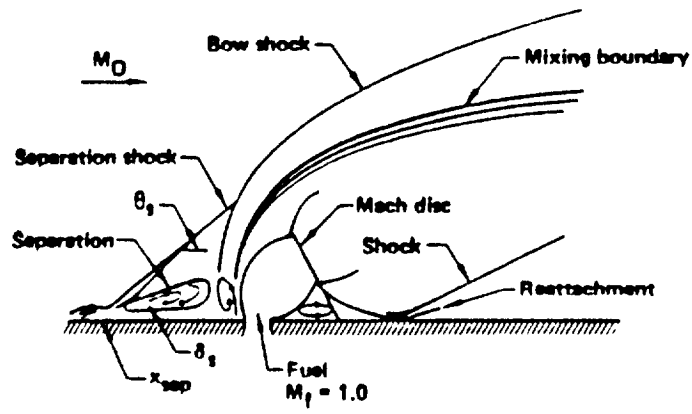
Figure 39. Schematic of normal fuel injector on flat plate.
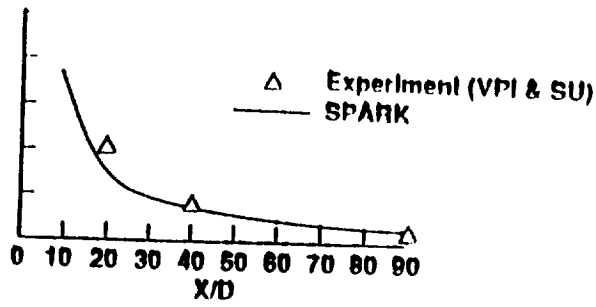
Figure 40. Maximum helium concentration versus axial
distance downstream of the injector (D-.00375m)
30 degree downstream injection.
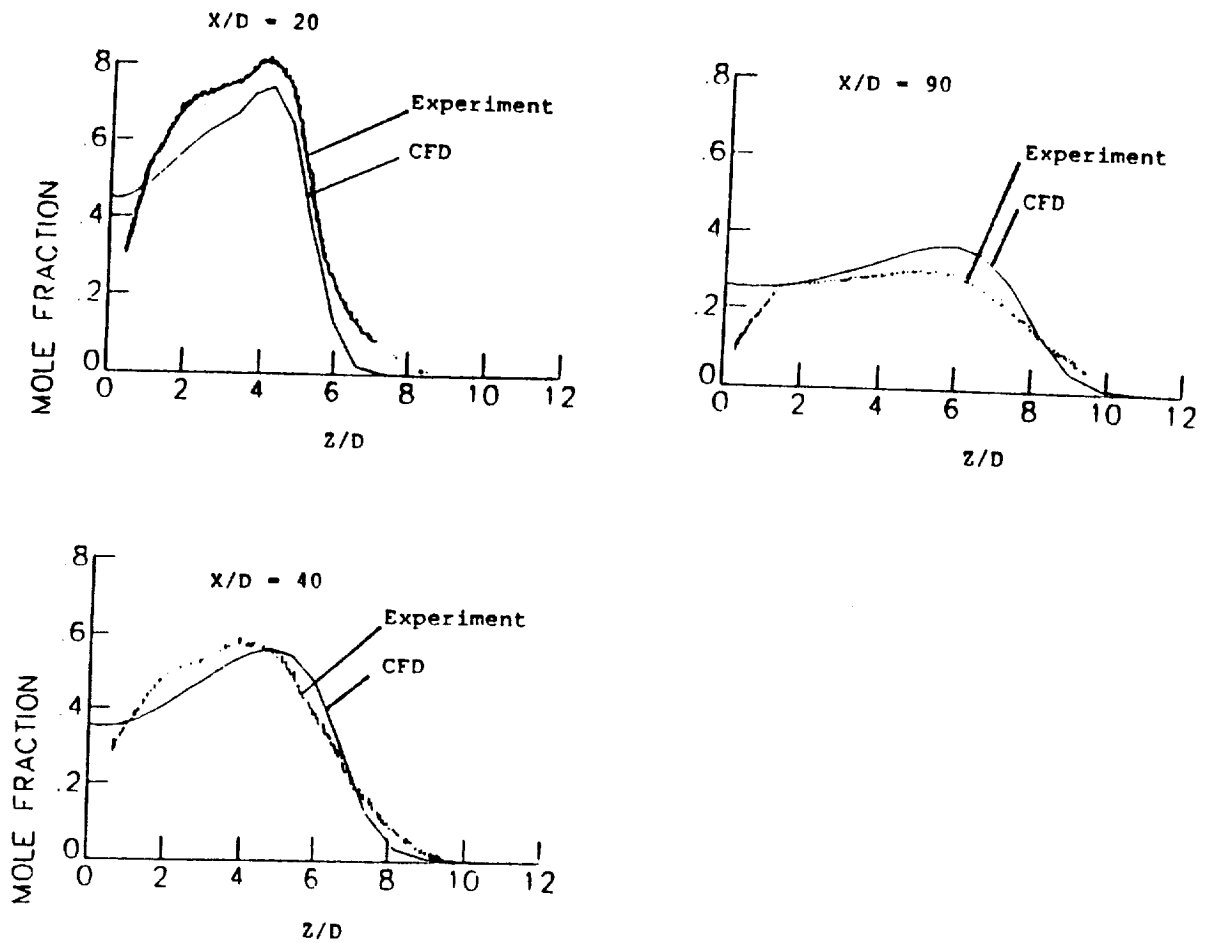
Figure 41. Computed versus experimental helium mole fraction
at jet centerline at three axial locations
(Z is vertical distance from plate)
30 degree downstream injection.
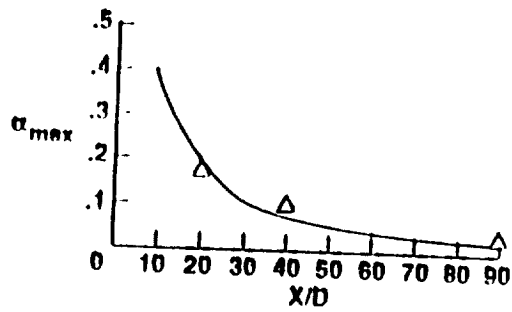
Figure 42. Maximum helium concentration versus axial
distance downstream of the injector (D=.00375m)
15 degree downstream injection.
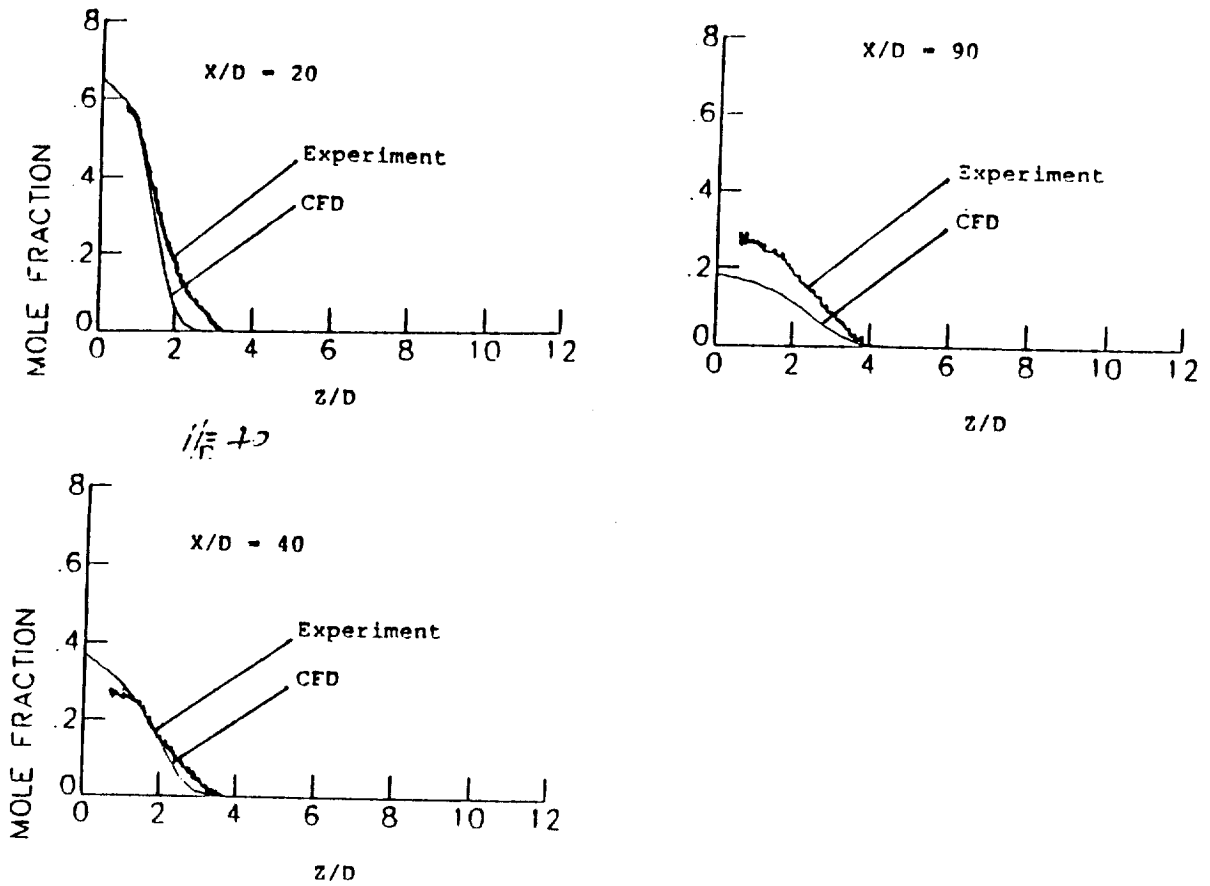
Figure 43. Computed versus experimental helium mole fraction
at jet centerline at three axial locations
(Z is vertical distance from plate)
15 degree downstream injection.
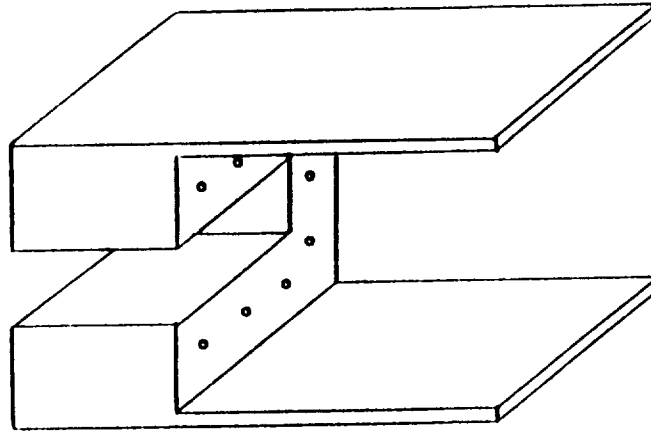
Figure 44. Generic scramjet combustor.
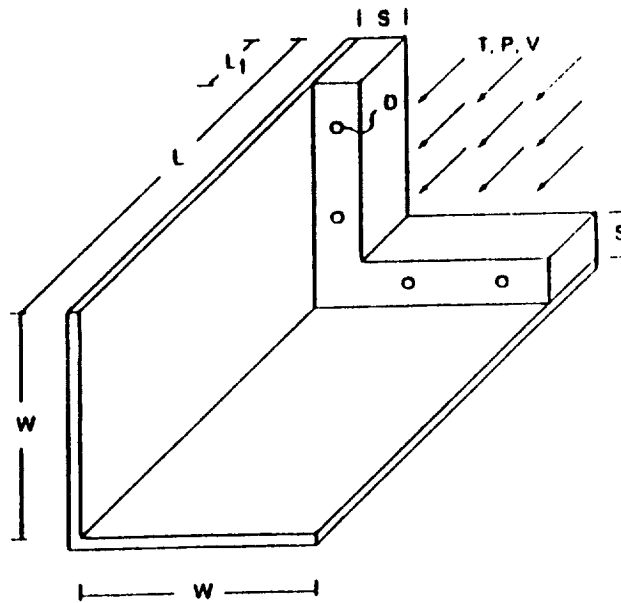
L = 20.0 cm, W = 10.0 cm
S = 2.0 cm, L_1 = 1.5 cm, D = 3.5 mm

Figure 45. Computational domain of generic scramjet combustor.
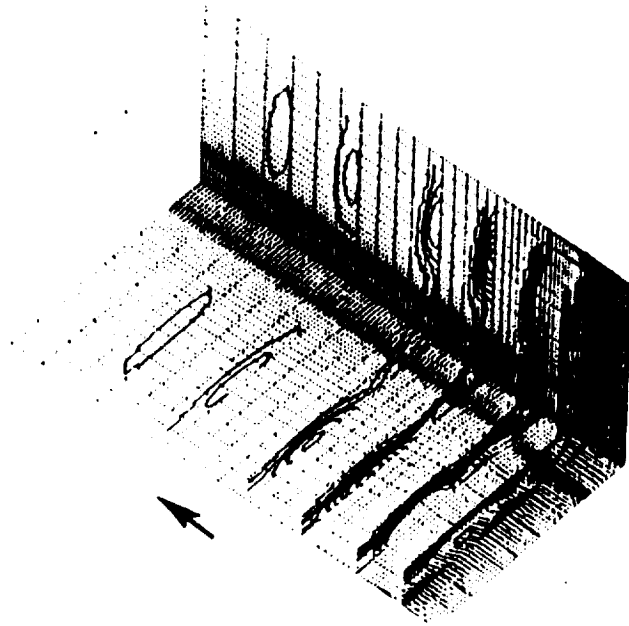
Figure 46. Hydrogen mass fraction contours in generic
scramjet combustor with four fuel injectors.
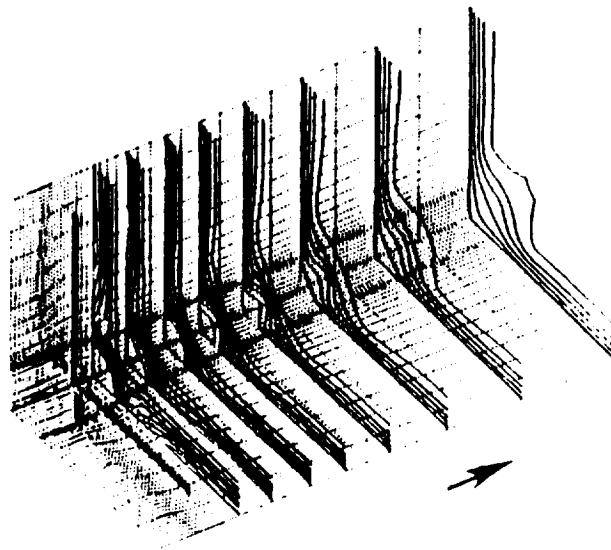
Figure 47. Streamwise velocity contours in generic scramjet
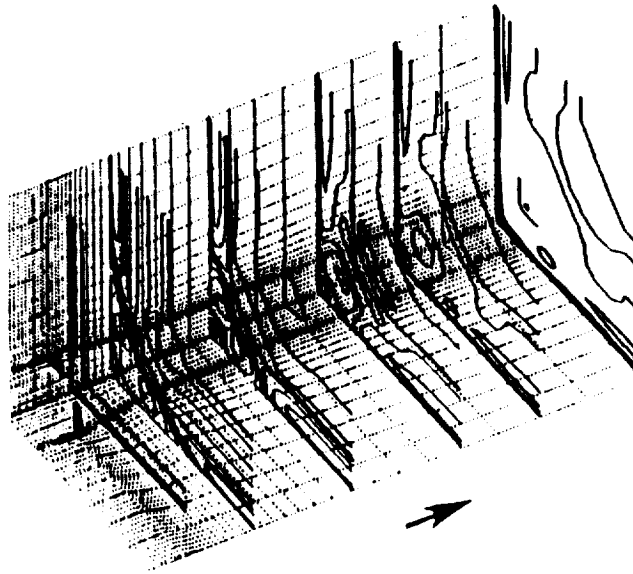
Figure 48. Temperature contours in generic scramjet combustor.
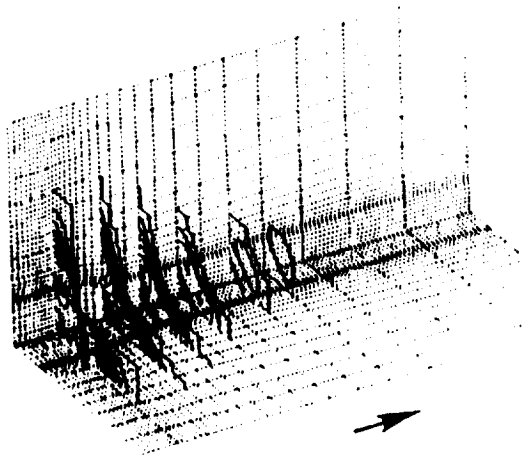
Figure 49. Hydrogen mass fraction contours in generic scramjet combustor.'

86
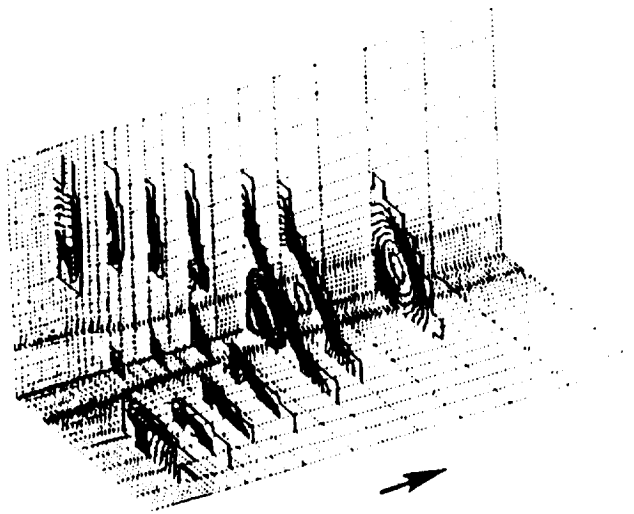
Figure 50. Water mass fraction contours in generic scramjet combustor.
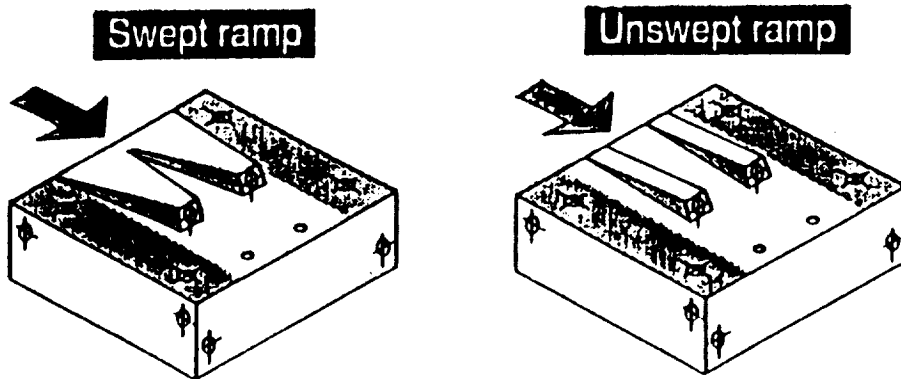
Figure 51. Swept and unswept ramp fuel injector configurations.
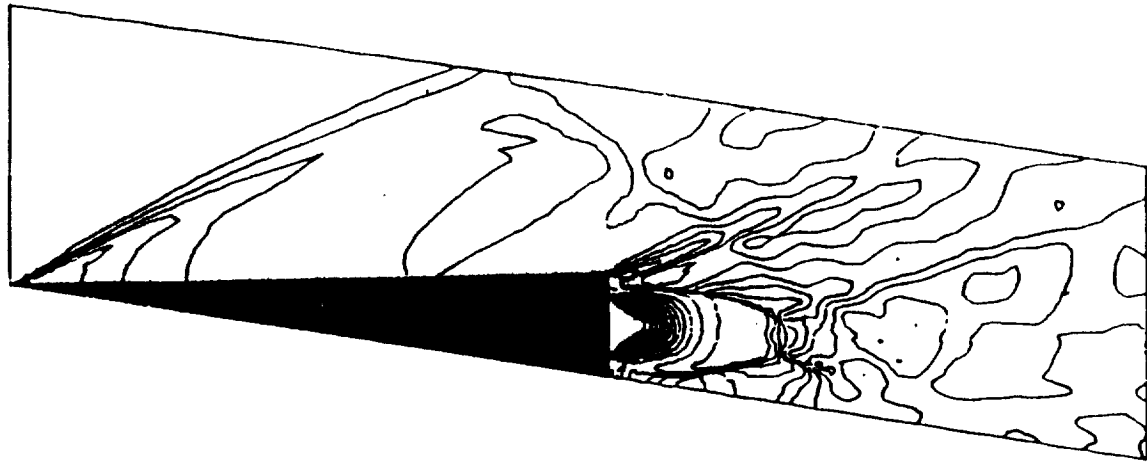
Unswept
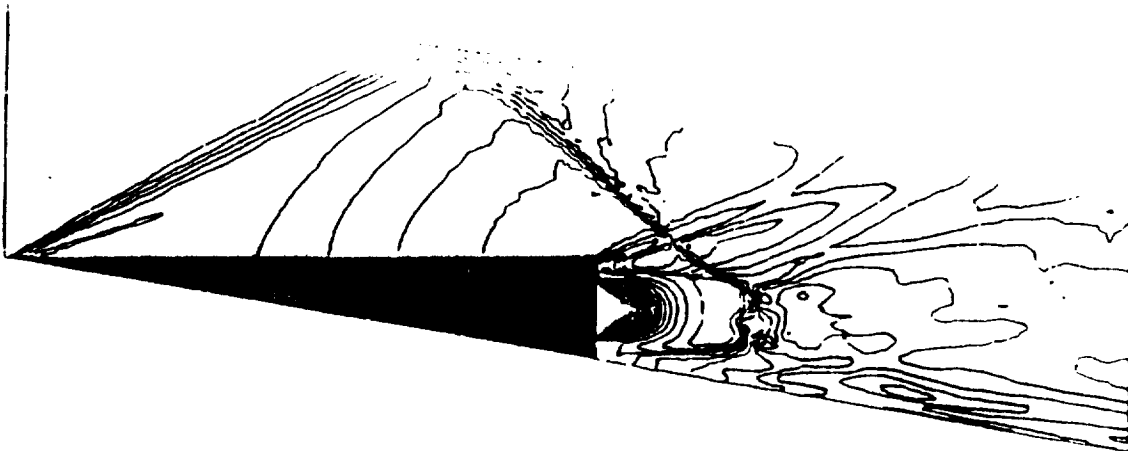
Swept

Figure 52. Pressure contours around ramp fuel injectors.
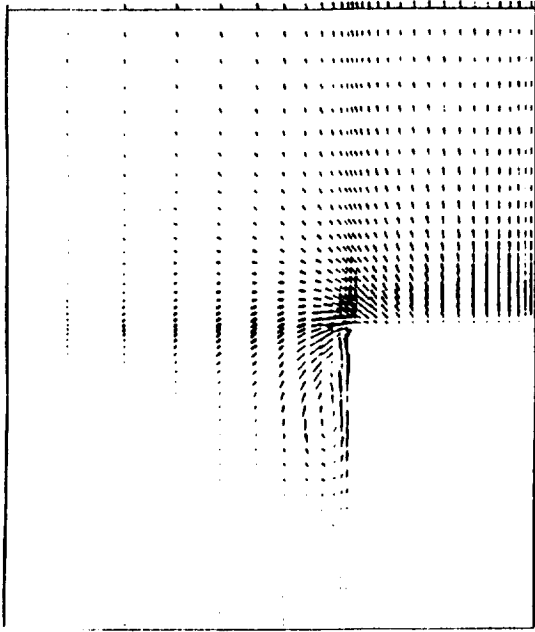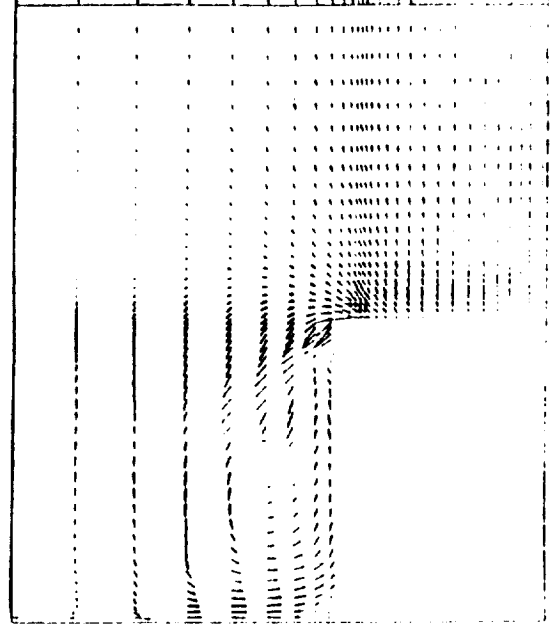
Unswept   Swept

Figure 53. Cross-stream velocity vectors at x = 6.60cm
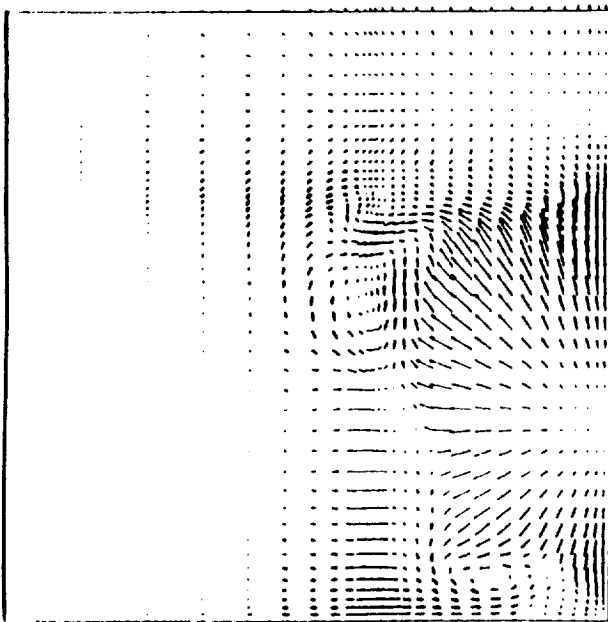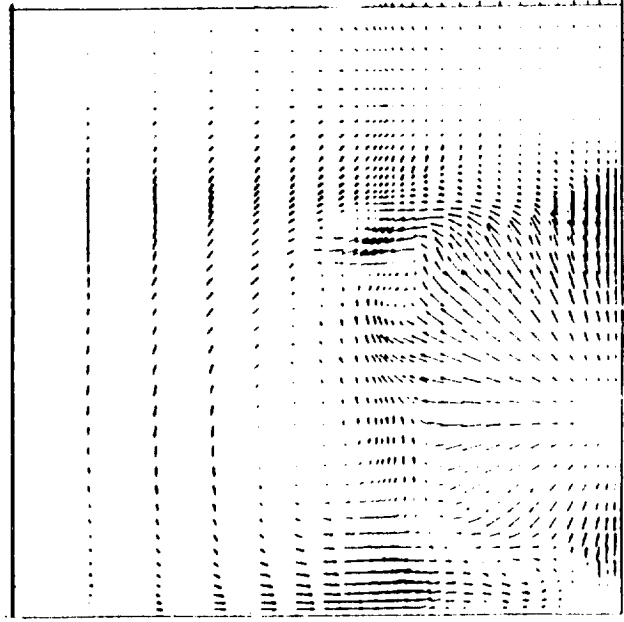
Unswept   Swept

Figure 54. Cross-stream velocity vectors at x = 8.06 cm
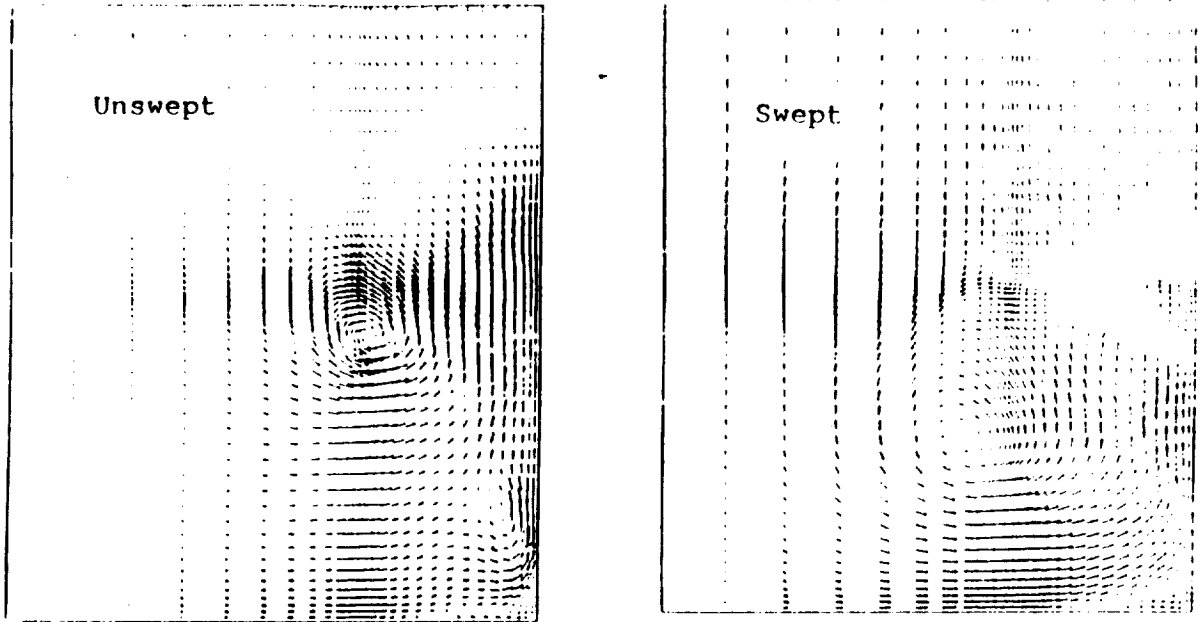
Figure 55. Cross-stream velocity vectors at x = 13.2 cm.
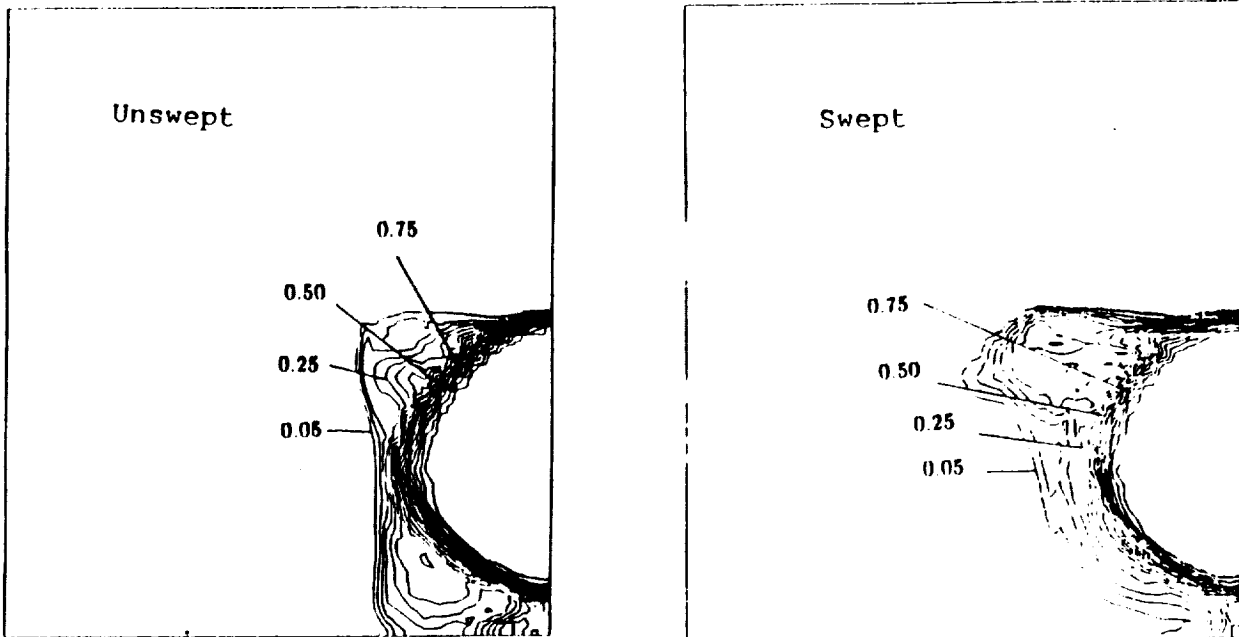
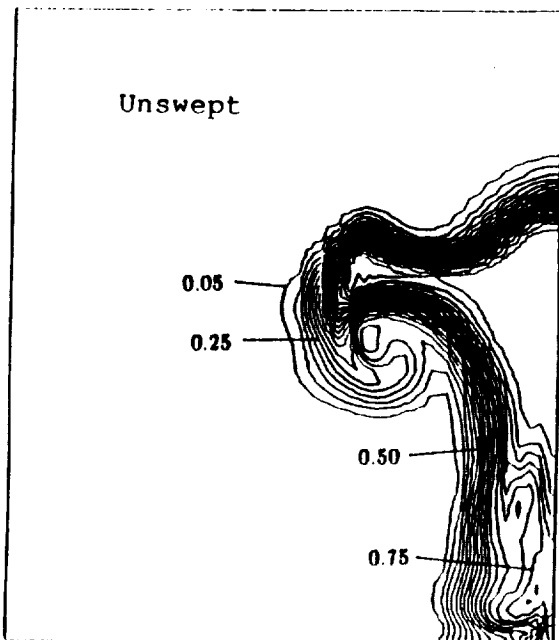Figure 56. Cross-stream hydrogen mass fraction contours
at x = 7.30 cm.
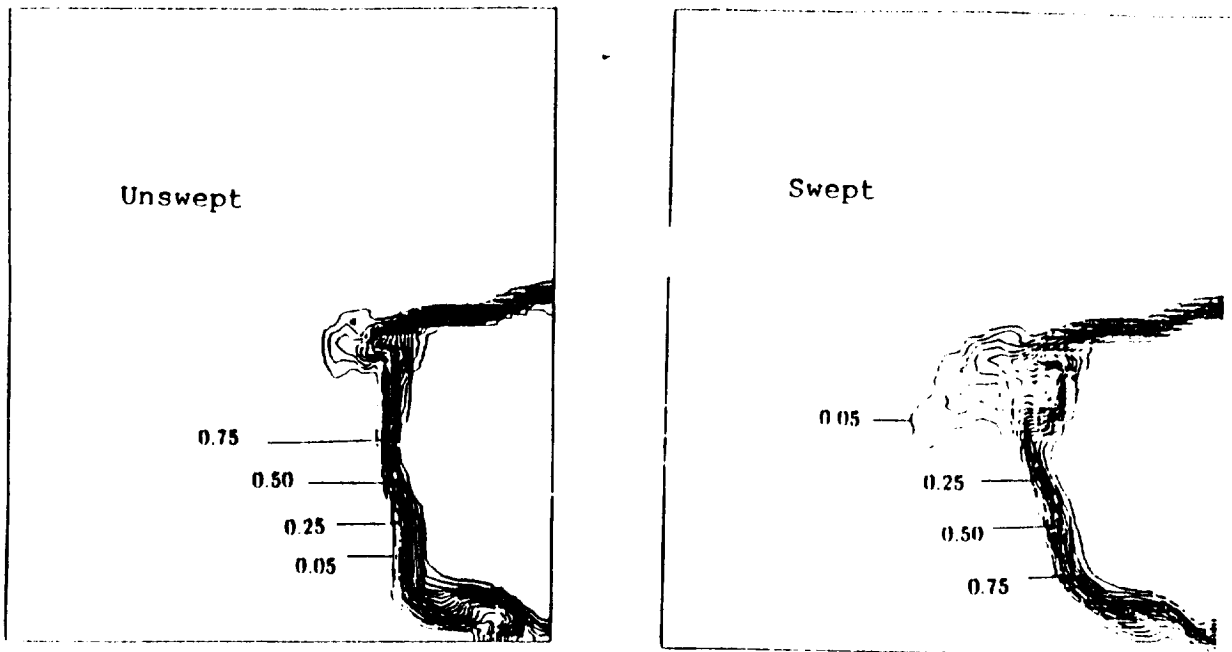
Figure 57. Cross-stream hydrogen mass fraction contours
at x = 8.06 cm.
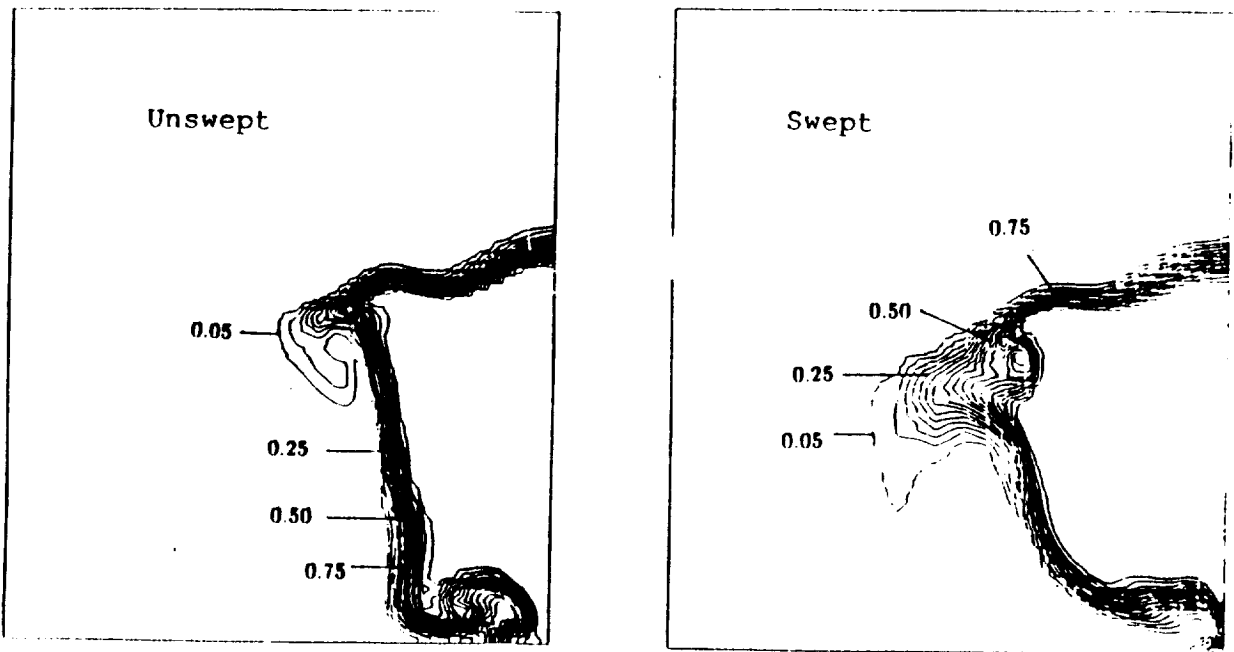
Figure 58. Cross-stream hydrogen mass fraction contours
at x = 9.6 cm.
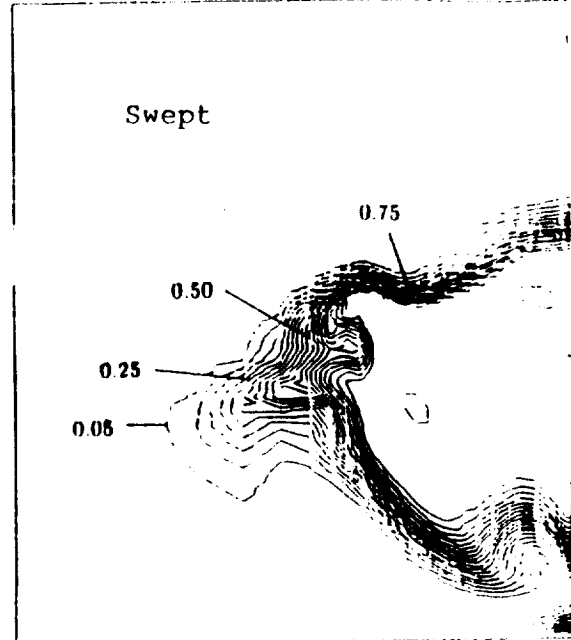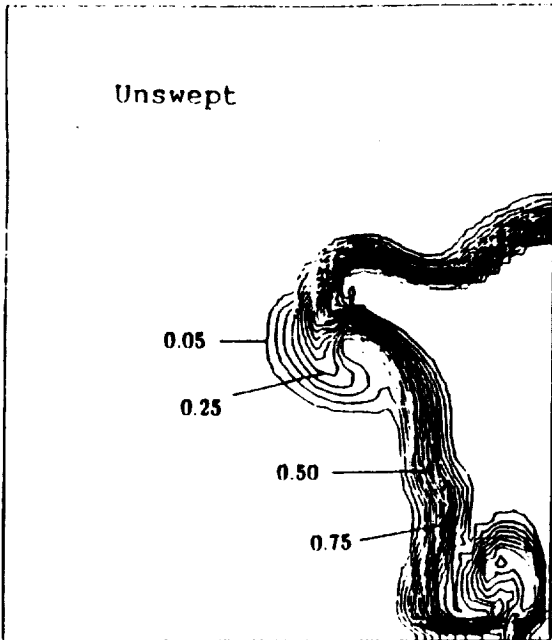
Figure 59. Cross-stream hydrogen mass fraction contours
at x = 11.3 cm.
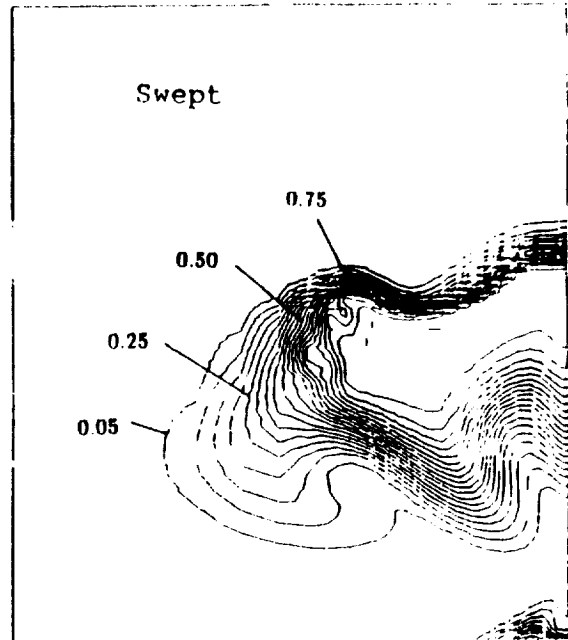
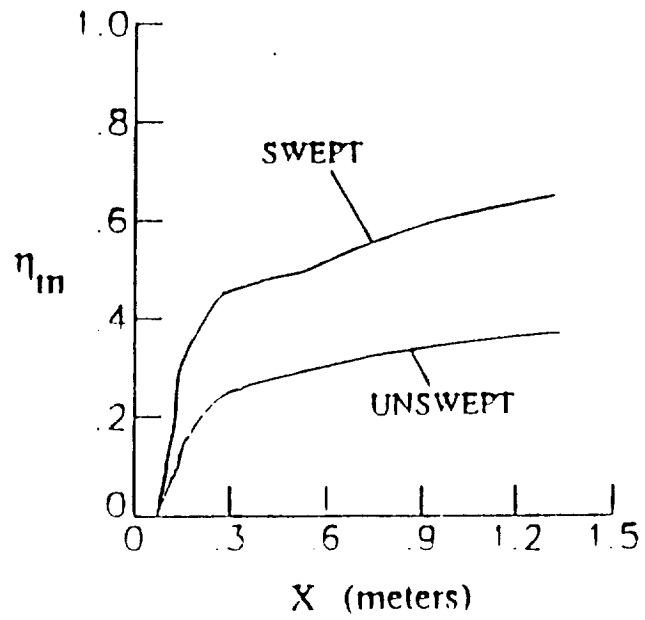Figure 60. Cross-stream hydrogen mass fraction contours
at x = 13.2 cm.

Figure 61. Mixing efficiencies for ramp injectors
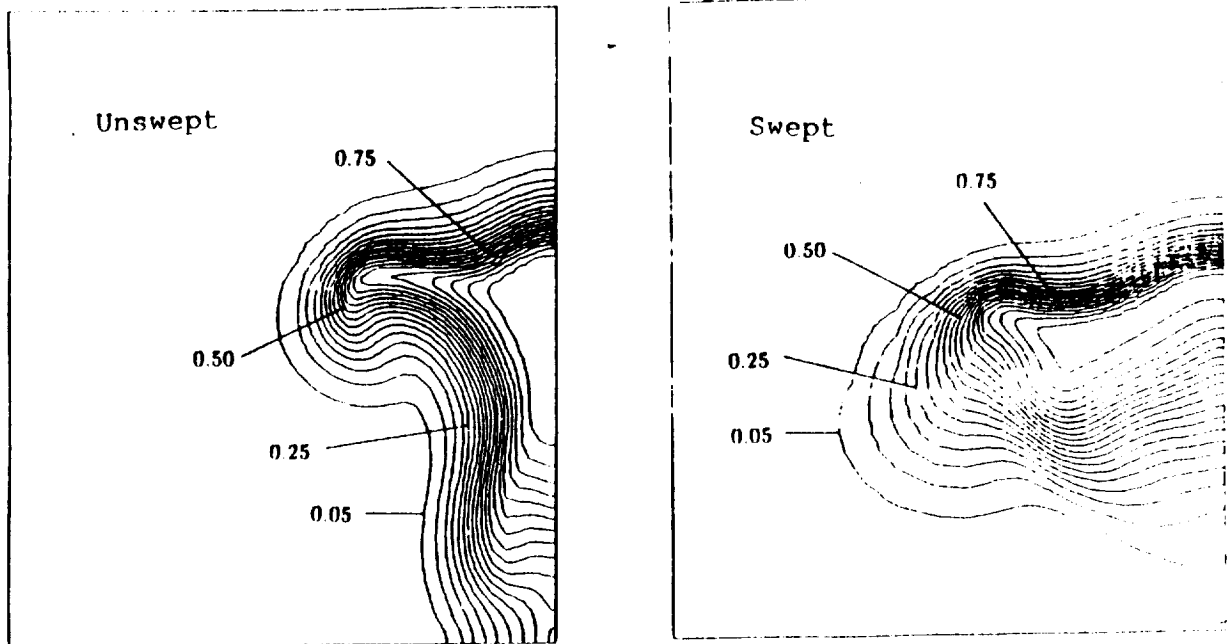

Figure 62. Cross-stream hydrogen mass fraction contours
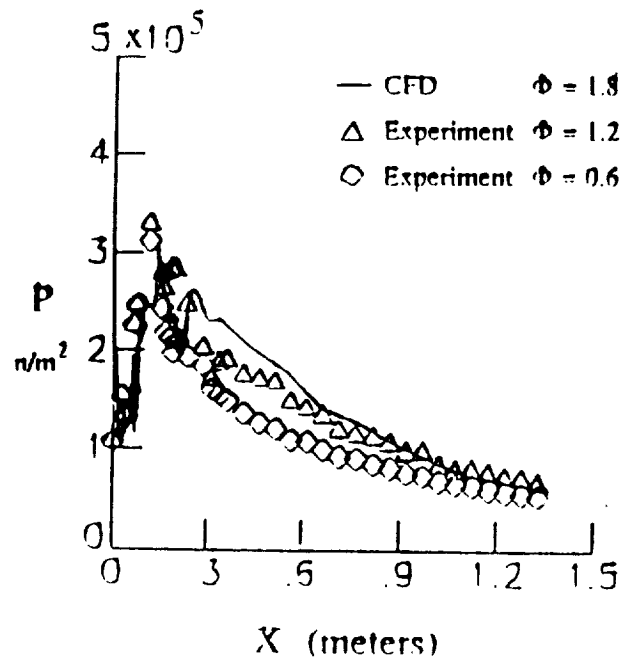with turbulent flow at x = 13.2.

Figure 63. Duct centerline wall pressure predictions versus experimental data for reacting swept ramp case.